

Characterizing Urban Planetary Boundary Layer Dynamics Using 3-Year Doppler Wind Lidar Measurements in a Western Yangtze River Delta City, China

Tianwen Wei¹, Mengya Wang^{1,2*}, Kenan Wu¹, Jinlong Yuan¹, Haiyun Xia^{1,2,3*}, Simone Lolli³, Lollo⁴

¹School of Atmospheric Physics, Nanjing University of Information Science & Technology, Nanjing 210044, China.

²China Meteorological Administration Xiong'an Atmospheric Boundary Layer Key Laboratory, Xiong'an New Area, Baoding 071800, China

³School³School of Earth and Space Science, University of Science and Technology of China, Hefei 230026, China

³CNR⁴CNR-IMAA, Contrada S. Loja snc, Tito Scalo (PZ), 85050, Italy

Correspondence to: Mengya Wang (wmengya123@nuist.edu.cn) and Haiyun Xia (hsia@ustc.edu.cn)

Abstract

The planetary boundary layer (PBL) dynamics play a critical role in shaping urban atmospheric processes by governing the exchange of energy, momentum, and mass within the lower atmosphere. Understanding the dynamics of the planetary boundary layer (PBL) is crucial for comprehending land-atmosphere interactions. This study utilizes three years of Doppler wind lidar measurements from June 2019 to June 2022 to investigate PBL dynamics over in Hefei, a city in the Western Yangtze River Delta, using three years (June 2019 to June 2022) of Doppler wind lidar data, China. We focus on the seasonal and diurnal variations in key parameters characteristics, such as including wind profiles, shear intensity, turbulent mixing, low-level jets (LLJs), and mixing layer heights (MLH), are analyzed. Results show that horizontal wind speeds accelerated more rapidly above 3 km, with the predominant westerly winds ($270^{\circ} \pm 15^{\circ}$) in all seasons. The vertical depth of high wind zone ($> 8 \text{ m s}^{-1}$) during the day is found generally deeper than at night, particularly in winter. In Hefei, LLJs primarily form at sunset and dissipate by noon, typically at altitudes between 0.5 and 0.6 km throughout the year, except in July. LLJ occurrences are most frequent in spring (31.7%), followed by summer (24.7%), autumn (22.3%), and winter (21.3%). Summer LLJs are most intensified, extending up to 1.5 km. The larger wind gradient below the jets significantly enhances turbulence and shear intensity near the ground at night. The seasonal average MLH peaks between 2:00 p.m. and 3:00 p.m., reaching approximately 1.2 km in spring and summer. Cloud cover raises MLH by about 100 m at night but decreases it by 200 m at the afternoon peak. This study provides insights into lidar-based PBL dynamics and highlights implications for local standards concerning low-altitude economic activities.

1. Introduction

The planetary boundary layer (PBL) refers to the lowest 1~3 km of the atmosphere that is directly influenced by the presence of the underlying surface, and typically usually responds to surface forcings

38 in an hour or less (Stull, 1988). These surface forcings include frictional drag, ~~heat exchange~~heat transfer,
39 pollutant emission, evaporation and transpiration, and terrain induced flow modifications (Garratt, 1994).
40 The depth and structure of the PBL are determined by the physical and thermal properties of the
41 underlying surface as well as the dynamics and thermodynamics of the lower atmosphere (Madala et al.,
42 2014; Barlow, 2014). One of the most important characteristic of the PBL is turbulence, which dominates
43 the vertical exchange of heat, moisture, momentum, trace gases, and aerosols between the free
44 atmosphere and the Earth's surface or regolith (Baklanov et al., 2011; Petrosyan et al., 2011). In the PBL,
45 the sources of turbulent mixing exhibit significant temporal and spatial variations, which include
46 buoyancy (convective mixing), wind shear (mechanical mixing), entrainment at the top of boundary layer,
47 and radiative cooling in stratocumulus clouds (top-down convective mixing) (Ortiz-Amezcuca et al.,
48 2022). Such turbulent motion in the PBL has been demonstrated to be inherently connected to air
49 pollution by modulating the dispersion, transport, and accumulation process, and have critical impacts
50 on land-atmosphere energy balance, as well as aerosol-cloud-precipitation-radiation interactions (Kim
51 and Entekhabi, 1998; Wang et al., 2001; Chen et al., 2011; Wood et al., 2015; Li et al., 2017; Su et al.,
52 2020, 2018; Pérez-Ramírez et al., 2019, 2021; Christensen et al., 2024).

53 Hefei, the capital of Anhui province, has experienced incredible economic growth and urban sprawl
54 over the past two decades (Zhao and Zou, 2018). Situated between the Yangtze River and Huaihe River,
55 in what is known as the Jianghuai region, the Hefei Metropolitan Circle plays a pivotal role in the Yangtze
56 River-Huaihe River Water Transfer Project to provide benefits for water supply, transportation,
57 agriculture, and power generation (Li et al., 2019; Zhang et al., 2023). Apart from tremendous economic
58 benefits achieved in Hefei, intense human activities create a profound influence on the local climate,
59 affecting the thermal, hydrological, and wind environments in the PBL within and beyond city limits (Shi
60 et al., 2008; Li et al., 2022a). In this context, the PBL study is vital for better understanding the exchange
61 process between the atmosphere and land over complex underlying surfaces, and improving the
62 parameterization schemes in numerical weather prediction models. However, previous studies mainly
63 focused on surface air pollution characteristics and its associations with meteorological parameters, as
64 well as the impacts on human health based on in-situ monitoring measurements or air quality modelling
65 (Hu et al., 2024; Qin et al., 2017; Shen et al., 2022; Zhang et al., 2017; Zhu et al., 2019). Among various
66 observation techniques, the lidar is a powerful tool and has been applied in retrieve vertical profiles of
67 PBL properties ~~in Hefei~~, such as aerosols, winds, turbulence, precipitation, temperature, and water vapor
68 during a period (Zhou, 2002; Xia et al., 2015, 2016; Wei et al., 2021, 2022, 2025; Jiang et al., 2022; Yuan
69 et al., 2020; Wang et al., 2015b). Therefore, it is essential to utilize the long-term lidar measurement to
70 characterize the PBL dynamics such as winds and turbulence sources to further understand the land-
71 atmosphere interaction.

72 The key parameter of PBL meteorology is the PBL height (PBLH) which displays significant
73 spatiotemporal variability under different atmospheric and surface conditions (Guo et al., 2019; Zhang
74 et al., 2022; Zhao et al., 2023). It strongly depends on surface characteristics such as surface heating rate,
75 strength of winds, topography, surface roughness, free atmospheric characteristics, the amount of clouds
76 and moisture (Kotthaus et al., 2023; Zhang et al., 2020). Multiple approaches have been developed to
77 determine the PBLH based on observations, such as in situ radiosonde (Gu et al., 2022; Guo et al., 2021;
78 Yue et al., 2021), aerosol-based and dynamic-based lidar techniques (Chen et al., 2022; Huang et al.,
79 2017; Vivone et al., 2021; Wang et al., 2020, 2021; Yang et al., 2020; Yin et al., 2019). In the practical
80 measurements of PBLH, it is necessary to consider its distinct diurnal cycle of PBL. The PBL can be
81 categorized into three dominant regimes: convective boundary layer (CBL), stable boundary layer (SBL),

82 and residual layer (RL) based on the thermodynamic stability in the lower atmosphere (Caughey and
83 Palmer, 1979). After sunrise, increasing radiative heating triggers the development of near-surface
84 turbulent eddies and leads to the formation of CBL, which ~~the CBL~~ grows with time and reaches its
85 ~~maximamaximum~~ in the early afternoon. The CBL consists of a convective surface layer, mixing layer
86 (ML) above, and entrainment zone (EZ) at the top (Wyngaard, 1988). After sunset, the radiative cooling
87 creates the SBL close to the surface and its depth grows as night progresses. The RL lies above the SBL
88 meanwhile a capping inversion overlies the RL (Fochesatto et al., 2001). However, studies in diurnal and
89 seasonal characteristics of the PBLH under different stable conditions in Hefei based on long-term
90 measurements have not been documented yet, to the best of our knowledge at the writing of this work.

91 Turbulence in the PBL is generated mechanically by wind shear, and convectively by buoyancy.
92 Wind shear is the main source of turbulence in the nocturnal boundary layer (NBL, also known as the
93 SBL), which can be enhanced in the presence of low-level jets (LLJs). Yang et al. (2023) found that wind
94 shears induced by LLJs often enhanced the vertical mixing processes, reduced the atmospheric stability,
95 and resulted in small weak direction shifts in eastern Idaho, USA. The formation of LLJ can provide a
96 driving force for the development of a deeper CBL on the Tibet Plateau (Su et al., 2024). Many studies
97 investigated the prominent role of LLJs in heavy rainfall events in the Jianghuai region (Chen et al., 2020;
98 Yan et al., 2021; Liu et al., 2022; Cui et al., 2023), but there has been a lack of research specifically
99 focusing on Hefei. The Huaihe River region, including Hefei, is one of the six high-frequency regions of
100 LLJs in China (Yan et al., 2021). The LLJs over China are usually classified into two types: boundary
101 layer jets (BLJs, below 1 km) and synoptic-system-related LLJs (SLLJs, within 1–4 km) (Du et al., 2014).
102 The occurrence of BLJs is associated with significant vertical shear of horizontal wind and diurnal
103 variation. On the contrary, SLLJs are usually related to synoptic-scale weather systems. This study
104 addresses a previous research gap by investigating the characteristics of LLJs formation and types, and
105 vertical wind shear (VWSH) in Hefei, with a focus on their monthly variations across different times and
106 altitudes.

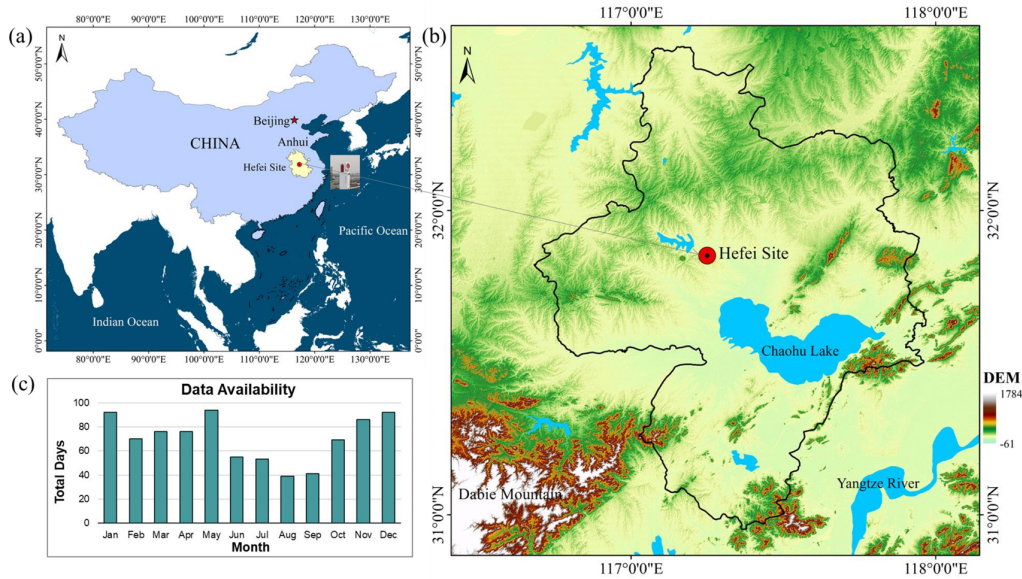
107 In this paper, we utilize a 3-year Doppler wind lidar ~~measurements~~measurements to characterize
108 the PBL dynamics in Hefei. The horizontal wind speeds and direction, LLJs, VWSH, turbulent kinetic
109 energy dissipation rate (TKEDR), mixing layer height (MLH) and PBLH are thoroughly analyzed.
110 Remote sensing retrieval of the above PBL parameters have been fully illustrated and validated in our
111 previous studies (Wang et al., 2019, 2021; Wei et al., 2019, 2022; Wang et al., 2024). This paper aims to
112 shed new light on the diurnal and seasonal characteristics of PBL meteorology and turbulence influenced
113 by diurnal cycles, general circulation, the Asian monsoon, and the synoptic systems.

114 2. Materials and methodology

115 2.1 Study area and instruments

116 Hefei, a rapidly developing new first-tier city, is located in Eastern China within central Anhui
117 Province in Figure 1(a). It covers an area of 11465 km², comprising four urban districts, one county-level
118 Chaohu city, and four counties. Its topography includes flat plains, gently rolling hills, and major water
119 bodies such as Chaohu Lake to the southeast in Figure 1(b). The city altitude mainly ranges from 15 to
120 81 m, with the highest point reaching 595 m (Sun and Ongsomwang, 2021). The Dabie Mountain in the
121 southwest introduces varied elevations and complex topographical features that influence regional
122 atmospheric dynamics in Hefei. Anhui province including Hefei, is located across both the eastern
123 monsoon region and the north-south climate transition zone of China. Hence, Hefei is characterized by

124 the typical subtropical monsoon climate with four distinct seasons. The city receives an annual
 125 precipitation of ~1000 mm and average temperature of 15.7 °C, with prevailing southeast winds in spring
 126 and summer and northwest winds in autumn and winter (Li et al., 2024).



127
 128 **Figure 1.** Study area and location of the Doppler wind lidar system. (a) Location (31.83°N, 117.25°E) of Hefei site
 129 and administrative boundary of Anhui province; (b) Digital Elevation Model (DEM), showing topographical features
 130 with DEM, and the solid black line representing represents the administrative boundary of Hefei city; (c) Data
 131 availability of 3-year Doppler wind lidar measurements. Total days with valid lidar measurements are accounted for
 132 each month.

133 **Table A1.** Key Operating Parameters of the Doppler Lidar System

Parameter	Value
Wavelength (nm)	1548
Pulse energy (μJ)	300
Pulse duration (ns)	600
Repetition rate (kHz)	10
AOM frequency shift (MHz)	80
Diameter (mm)	100
Sampling frequency (MHz)	250
Range gate length (m)	30/60/150
Radial time resolution (s)	1
Scanning mode	VAD
Elevation angle (°)	60
Azimuth angle (°)	0-300

134
 135 A compact coherent Doppler wind lidar (CDWL) system was deployed on the roof of the School of
 136 Earth and Space Science (SESS) building of the University of Science and Technology of China (31.83°
 137 N, 117.25°E) in the urban area of Hefei, to monitor the vertical profiles of aerosol, cloud and wind field.
 138 The lidar location is denoted as the Hefei site in Figures 1(a) and 1(b)The specific location of lidar is
 139 referred as Hefei site in Figure 1(a) and Figure 1(b). The lidar system operates at 1.5 μm eye-safe
 140 wavelength and uses 300 μJ pulse energy and 10 kHz repetition rate to achieve a maximum detection
 141 range of up to 15 km. During the long-term experiment, the lidar performed continuous velocity azimuth
 142 display (VAD) scanning mode for high spatial-temporal resolution wind profile measurement. The
 143 azimuth angle ranges from 0° to 300° with an interval of 5° and the elevation angle is 60°. The key

operating parameters of the Doppler lidar system are summarized in Table A1 in Appendix. Detailed information about the validation and application of the lidar system can be found in our previous works (Jia et al., 2019; Wei et al., 2020, 2021). The data availability is presented in Figure 1(c) with monthly statistics of total valid days. Note that the lower data availability during the summer seasons is primarily due to frequent rainfall and high temperatures, which caused instability in the lidar systems. However, these issues have been significantly improved in the recently updated systems (Xia et al., 2024).

2.2 Datasets and methods

The CDWL system operated for three consecutive years from June, 2019 to June, 2022, except for some maintenance interruptions (Wang et al., 2024). Table 2 presents the number of available observation days for each season and weather type. The number of days available for different seasons and weather types is presented in Table 1, respectively.

Table 12. Observation days by weather type during Doppler lidar operations. The days of different weather types during the period of Doppler lidar operation

Weather Types*	Spring	Summer	Autumn	Winter	Total days
Rainy	62	44	37	75	218
Clear	69	21	47	76	213
Cloudy	68	82	50	64	264
Partly Cloudy	39	38	44	39	160

***Rainy:** rain persists for more than 2 hours **Clear:** clouds are present for less than 2 hours.

Cloudy: cloud coverage exceeds 8 hours. **Partly Cloudy:** cloud coverage lasts between 2 to 8 hours.

The time resolution and range gate resolution of the original radial measurements are 1 s and 30 m, respectively. Horizontal wind speed (HWS), horizontal wind direction (HWD), and vertical wind speed (VWS) are retrieved from the measured radial speeds at different azimuth angles using a filtered sine-wave fitting method, based on the assumption of horizontally homogenous wind field (Smalikho, 2003; Banakh et al., 2010; Wei et al., 2020). Considering the duration of one VAD scan, the time resolution of wind profile becomes about 2 minutes. Here, the wind direction of 0° represents the horizontal wind coming from the north, and the angle increases clockwise. The negative (positive) vertical wind speed was defined as upward (downward) motion in this study.

Turbulence activity can be expressed by vertical velocity variance, spectrum width, turbulent kinetic energy, and TKEDR (O'Connor et al., 2010). In this study, we estimate TKEDR using the turbulence statistical model based on the relation between the structure-function of the measured radial velocity and theoretical value (Banakh et al., 2017). The MLH is a significant parameter for presenting the vertical turbulent exchange within the PBL. On the basis of the characteristics of decreasing convective turbulence intensity along with height, the threshold method can effectively determine a typical turbulence height. Here, the MLH is defined as the height up to which $TKEDR > 10^{-4} \text{ m}^2 \text{ s}^{-3}$ is reached (Banakh et al., 2021; Wang et al., 2021). In addition, the aerosol-based PBLH, shown in Section 3.6, is also calculated for comparison. It is determined from the aerosol backscatter coefficient using a Harr wavelet method (Caicedo et al., 2017; Kotthaus et al., 2023).

LLJ is a fast air stream with a wind speed maximum in the lowest kilometers of the troposphere (Stull, 1988). Referring the previous studies (Qiu et al., 2023; Zhang et al., 2018; Tuononen et al., 2017) and considering the local characteristics, we identify the LLJs at Hefei using the following criteria: (1) the maximum wind speed $U_{max} > 8 \text{ m s}^{-1}$ and, (2) the wind speed difference $\Delta U = U_{max} - U_{min} > 2.6 \text{ m s}^{-1}$, where U_{min} is the minimum wind speed above the height of U_{max} . The LLJ height is then

182 defined as the height of U_{max} . In addition, when a two-layer LLJ exists, the lower one will be selected.
 183 Each wind profile was applied to identify the LLJ event. In the statistics procedure of Section 3.3, a time
 184 window of 1 h is used to filter out the outliers, and those with fewer than 60% within the window were
 185 abandoned.

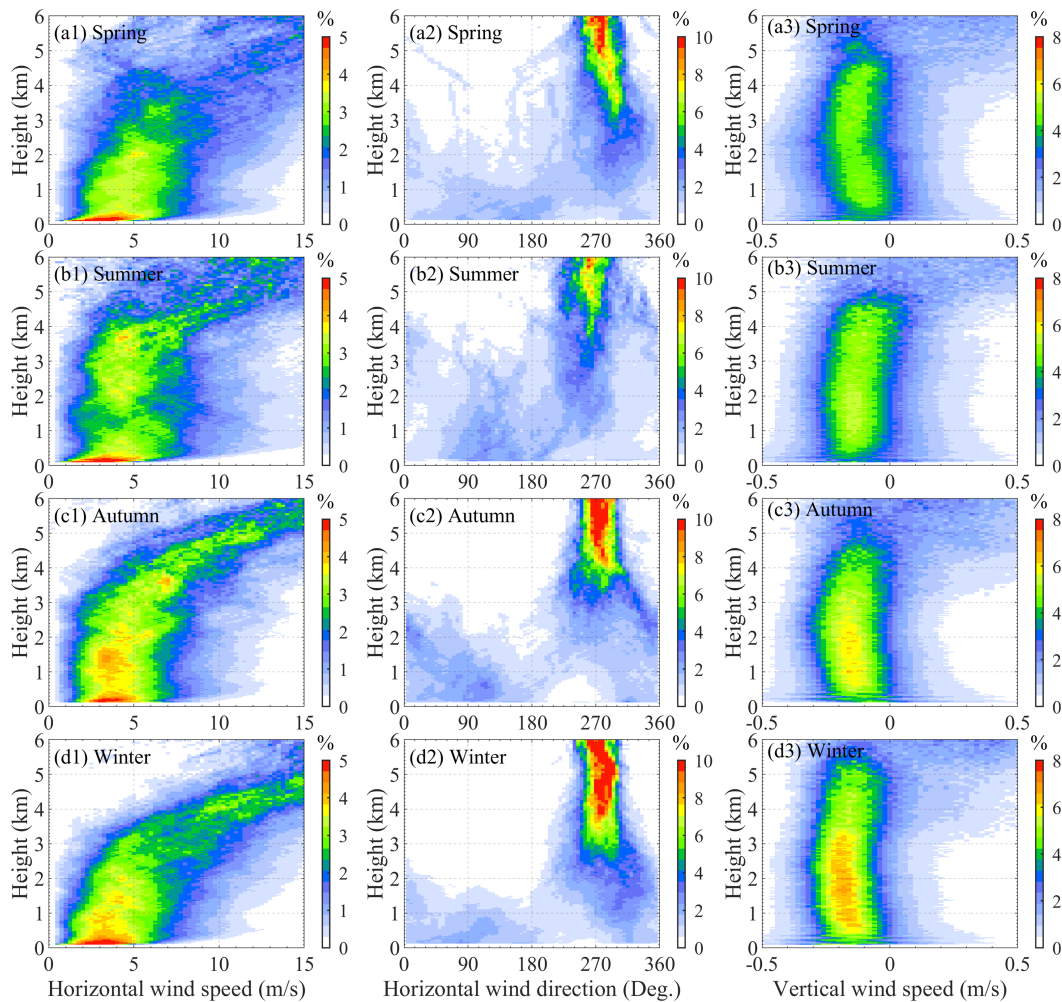
186 Vertical wind shear (VWSH) is defined as the change in wind speed and/or direction with height. It
 187 can be calculated from the vertical wind profiles using the following equation (Manninen et al., 2018)

188
$$\text{VWSH} = \frac{(\Delta u^2 + \Delta v^2)^{0.5}}{\Delta z}$$

189 where the difference in vectors of the wind components u and v is divided by the height difference Δz
 190 between the two altitude levels used to compute the wind shear.

191 3. Results

192 3.1 The 3-year seasonal profiles of the wind frequency



193
 194 **Figure 2.** The seasonal frequency distributions of (a1-d1) horizontal wind speed (left panel), (a2-d2) horizontal
 195 wind direction (middle panel), and (a3-d3) vertical wind speed (right panel) at different heights below 6 km in Hefei.
 196 Panels (a-d) represent spring (Mar-May), summer (Jun-Aug), autumn (Sep-Nov), and winter (Dec-Feb),
 197 respectively during (a) Spring: Mar-May; (b) Summer: Jun-Aug; (c) Autumn: Sep-Nov; and (d) Winter: Dec-Feb, at
 198 Hefei. Frequencies along the x-axis are normalized to 100% at each height. Note that the sum of all frequency values
 199 along the x-axis equals 100% at any specific height. It should be noted that a negative vertical wind speeds indicate

200 ~~upward motion. egative value of vertical wind speed is defined as the upward movement of air.~~

201 Vertical wind profiles are influenced by surface friction, terrain, local pressure systems, and global
202 atmospheric circulation patterns. We retrieve the vertical profiles of HWS, HWD, and VWS and calculate
203 the frequency (%) of their occurrence at different heights above ground level (AGL), as shown in Figure
204 2. ~~The frequency distribution represents the ratio of wind speeds within each x-axis bin to the total valid~~
205 ~~counts at a given height~~~~The frequency distribution is calculated by the ratio of the counts of wind speeds~~
206 ~~falling into each bin on the x-axis to the total valid numbers at each height.~~ Therefore, the sum of all
207 frequency values along the x-axis is 100% at any specific height. To represent rich details, the bin size
208 or resolution (i.e., the width of each column) is set to 0.25 m s^{-1} , 5° , and 0.02 m s^{-1} for HWS, HWD, and
209 VWS, respectively.

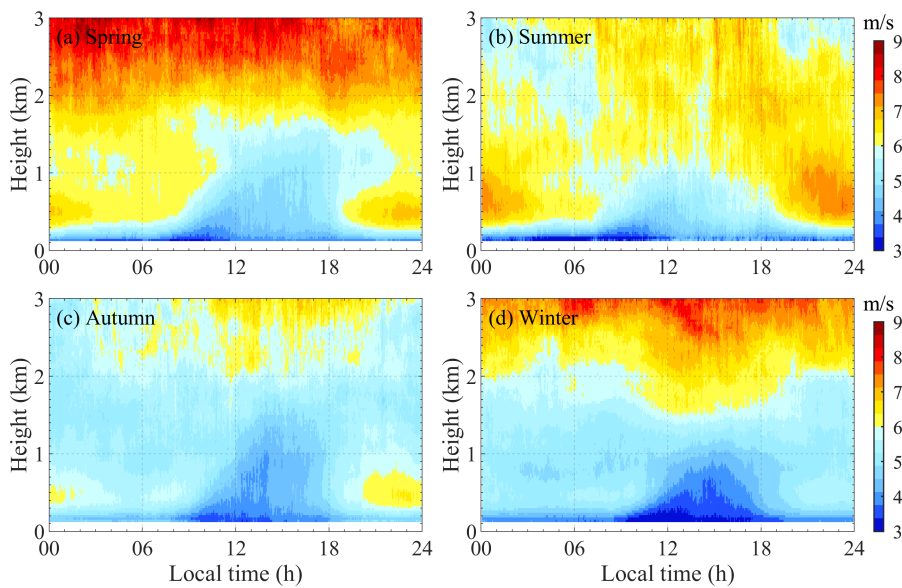
210 In the left panel of Figure 2, the frequency distribution of HWS (hereafter referred to as HWS%)
211 exhibits a rightward skew in all seasons, a characteristic often modeled using a Weibull or Lognormal
212 distribution due to the non-negative nature of wind speed (Justus et al., 1978; Pobočíková et al., 2017).
213 Close to the ground, the majority of HWS values are clustered at the lower end, mainly as a result of
214 surface friction. Below $\sim 300 \text{ m}$ AGL, HWS ~~increase~~~~increases~~ rapidly as surface friction decreases. From
215 300 m to 3 km AGL, HWS increases steadily while becoming more dispersed, with the overall
216 distribution (HWS%) spanning between 2 and 7 m s^{-1} . Above 3 km , HWS accelerates more rapidly,
217 particularly in autumn and winter, where HWS% remains relatively concentrated. In contrast, HWS% in
218 spring and summer is more dispersed with a lower frequency of high HWS occurrences ($> 10 \text{ m s}^{-1}$).
219 Many studies have demonstrated a significant decrease trend of near surface wind speed in eastern China
220 including Anhui province, induced by large-scale circulation and local land use and land cover change
221 (Li et al., 2018; Liu et al., 2023; Li et al., 2022). Wang et al. (2015) observed that the value of annual
222 mean surface wind speed in Hefei city during 1981-2012 was between 2.0 m s^{-1} and 2.6 m s^{-1} and the
223 highest frequency of maximum surface wind speed occurred in spring. A recent study by Li et al. (2022a)
224 analyzed the maximum daily wind speed of 10 minutes from 51 meteorological stations in Anhui
225 province from 2006 to 2020, which showed that the average maximum wind speed in the city of Hefei
226 was between $9.1\sim 17.6 \text{ m s}^{-1}$. Therefore, our results of seasonal HWS values near the ground correspond
227 to previous studies.

228 The frequency distribution of HWD (hereafter referred to as HWD%) exhibits distinct vertical
229 characteristics, as shown in the middle panel of Figure 2. At higher altitudes ($> 3 \text{ km}$), the distribution of
230 HWD is much more concentrated, with predominant westerly winds ($270^\circ \pm 15^\circ$) in all seasons. Because
231 Hefei city is located between $31^\circ 4' \text{ N}$ and $32^\circ 38' \text{ N}$, which is affected by westerly circulation. The finding
232 of prevailing westerlies throughout the year in Hefei is consistent with (Sun et al., 2021). In contrast, the
233 influence of westerly on HWD% below the PBL is insignificant due to the impact of the underlying
234 surface roughness, terrain distribution, and air flow turbulence. Below 3 km AGL, we can discover
235 notable southwest winds in summer compared to the other seasons. In the summer monsoon season,
236 eastern China (including Hefei city) is mainly dominated by southwest winds, as has been reported by
237 many studies (Liu et al., 2015; Yan et al., 2022; Zhao et al., 2007). Wind directions in the PBL tend to be
238 more variable and chaotic compared to those at higher altitudes. And westerly winds above 1.5 km
239 consistently strengthen with increasing altitude in all seasons.

240 The right panel of Figure 2 illustrates seasonal profiles of VWS frequency (hereafter referred to as
241 VWS%). The frequency distribution of VWS% is right-skewed and its center lay in negative values
242 between -0.2 m s^{-1} and -0.1 m s^{-1} . The results show that most VWS values are negative below 5 km in all
243 seasons, representing upward motion in the atmosphere. It demonstrates the asymmetric nature of vertical

244 velocities in the atmosphere, where upward movements are stronger than downward movements
 245 (Tamarin-Brodsky and Hadas, 2019). Furthermore, Figure 2 (d3) shows that winter has the highest
 246 frequency of negative VWS, with most VWS% ranging from 4% to 7% below 3 km AGL. A climatology
 247 study of cold frequency suggests that cold fronts are most frequently occurred in cold seasons over Hefei
 248 city (Xue et al., 2022). In winter, cold fronts associated with the winter monsoon can enhance upward
 249 motion of the air as the heavier (more dense) cool air pushes under the lighter (less dense) warm air
 250 (Kang et al., 2019; Parsons, 1992). The upward motion intensifies and is vigorous along the frontal
 251 boundaries, leading to cloud formation and precipitation. The higher positive values in the asymmetric
 252 distribution of VWS, particularly above 3 km, are attributed to the contribution of falling precipitation
 253 particles (Wei et al., 2019). Under these conditions, the detected vertical speed reflects the movement of
 254 larger hydrometeors rather than the air motion itself.

255 3.2 Diurnal HWS profiles in different seasons



256
 257 **Figure 3.** Diurnal profiles of seasonal-averaged horizontal wind speeds at different heights below 3 km. Time-height
 258 diagrams of seasonal average horizontal wind speed profiles below 3 km, during (a) Spring: Mar-May; (b) Summer:
 259 Jun-Aug; (c) Autumn: Sep-Nov; and (d) Winter: Dec-Feb, at Hefei.

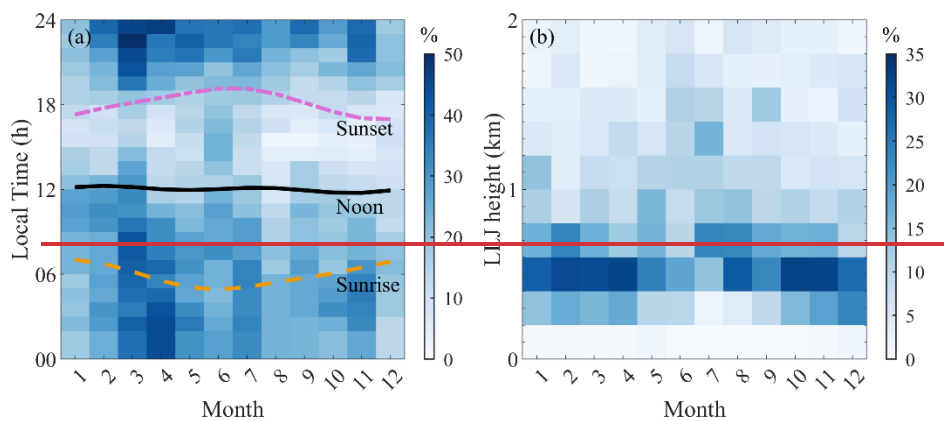
260 The diurnal variation of the vertical wind profile within the PBL is intricately linked to the dynamics
 261 and thermodynamics driven by the daily cycle of solar heating and longwave cooling. Figure 3 illustrates
 262 how HWS profile varies with local time (LT) on a seasonal scale. Minimum HWS values are observed
 263 near the surface due to the influence of surface roughness. ~~The minimum values of HWS are found in the~~
 264 ~~lowest layer, primarily due to the impact of rough surface.~~

265 During the day, solar heating induces turbulence and convection, which ~~increase~~ increases surface
 266 friction and ~~slows~~ slows down the up-level horizontal wind. This results in the formation of a gentle wind
 267 zone (GWZ), characterized by wind speeds below 5 m s^{-1} , a feature that can be observed in all seasons.
 268 And the diurnal variation of the GWZ strongly correlates with the development of the mixing layer. At
 269 night, radiative cooling generates a temperature inversion, inhibiting vertical mixing and fostering
 270 laminar flow with increased shear intensity. Consequently, nocturnal winds are generally stronger than
 271 daytime winds at the same height below 1.5 km AGL throughout all seasons. Above this height, the HWS
 272 profile is usually more uniform and stronger due to the reduced frictional drag in the free atmosphere. It

273 is interesting to find that the vertical height of high wind zone ($> 8 \text{ m s}^{-1}$) during the day is much lower
 274 than at night, particularly in winter. In Figure 3d, an appreciable enhancement of HWS at 1.5 km is
 275 discovered during the day particularly between 11:00 a.m. and 16:00 p.m., when the PBL tends to grow
 276 and become deeper due to radiative heating of the surface. In general, the HWS increases with height.
 277 However, as seen in Figures 3(a) to 3(c), a distinct local maximum in HWS, occurring between
 278 approximately 0.4 km and 0.8 km, is observed after 8:00 p.m. and before 7:00 a.m. the next day. This is
 279 especially pronounced in summer, where the highest values and the highest vertical extent of the wind
 280 are recorded. These winds are typically associated with the nocturnal LLJs, a narrow band of strong
 281 winds that forms in the lower PBL. Although the seasonal average HWS reflects the overall wind
 282 conditions, the pronounced notch structure in the profile underscores the frequent occurrence of LLJs,
 283 which will be explored in more detail in the next section.

284 3.3 Monthly characteristics of LLJ at different times and heights

285 LLJ is characterized by a concentrated band of strong winds located in the lower part of the
 286 atmosphere. The diurnal variation of its formation and occurrence is influenced by the interaction
 287 between surface heating/cooling cycles, atmospheric stability, and synoptic-scale weather patterns.
 288 Figure 4(a) illustrates the statistical frequency (%) of the occurrences of LLJs at different hours for each
 289 month. Frequency values are calculated as the ratio of the total number of LLJ occurrences to the total
 290 number of available days in the specific month over a 3-year period. Additionally, the monthly variation
 291 of the sunrise, noon, and sunset time was also plotted. Figure 4(b) presents the frequency distribution (%)
 292 of LLJs occurrences over the height for each month, with the sum of each column equaling 100%. The
 293 seasonal wind rose charts of the LLJ events ~~for the four seasons~~ are presented in Figure 5(a)-(d),
 294 ~~respectively~~. The seasonal and intraseasonal variability of predominant wind directions and wind speeds
 295 of LLJs are influenced by general circulation, the East Asian monsoon, and synoptic systems. The spatial
 296 distributions of the 500 hPa geopotential height and geopotential height anomalies are presented in
 297 Figure A1.



298

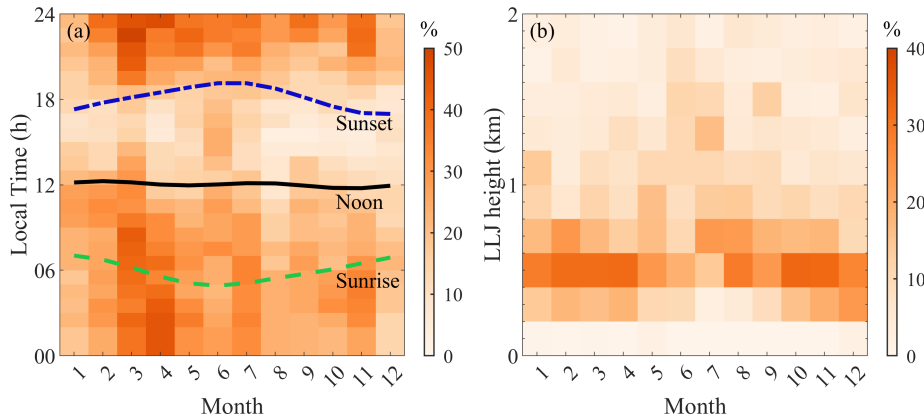


Figure 4. (a) Monthly frequency (%) of LLJ occurrences over time at different times for each month. The blue dot-dashed line indicates the mean sunset time, the black solid line marks noon, and the green long-dashed line represents sunrise. (b) Height distribution of LLJ occurrence frequency by month, with normalized column totals (100%).

As shown in Figure 4(a), generally, the results indicate that LLJs occur most frequently in spring, followed by summer, autumn, and winter in Hefei, which aligns with findings by Yan et al. (2021) based on long-term radiosonde observations, who found that LLJs were the most frequent in spring in the Huaihe River Basin based on long-term radiosonde observations from 2011 to 2017. The seasonal average frequency of LLJ occurrences is highest in spring (31.7%), followed by summer (24.7%), autumn (22.3%), and winter (21.3%). The average seasonal LLJ frequencies were 31.7%, 24.7%, 22.3%, and 21.3% in spring, summer, autumn, and winter, respectively. In Figure 4(a), the sunrise and sunset times exhibit monthly variation due to the Earth's revolution around the Sun. We refer to the period between sunset and sunrise as daytime, and the period between sunset and the next sunrise as nighttime. LLJs are predominantly more frequently observed during the night and early morning throughout all months the year. According to the classical theoretical description of inertial oscillations, nocturnal LLJs (NLLJs) develop from because of due to the decoupling of nocturnal winds from the surface friction, facilitated by the formation-development of a near-surface temperature inversion (Blackadar, 1957). At night, the surface-ground cools more rapidly than the air above, giving a rise to the formation of temperature inversions. This inversion effectively reduces the influence of surface frictional on the air above it-the temperature inversion to decouple from the surface's frictional effects (Mirza et al., 2024). The weaker-reduced friction enables-allows the wind aloft to an-acceleration-of-wind-aloft-with, leading to the development of a pronounced super-geostrophic wind speed maximum. Such undisturbed inertial oscillations are a-widely recognized as a primary-known formation-mechanism of-for the formation of Nocturnal-LLJ (NLLJ) (Sisterson and Frenzen, 1978). LLJs are typically often-most pronounced during the early morning hours, just typically-before the onset of daytime heating. During this time, when the temperature inversion is typically-strongest because due to prolonged nocturnal cooling-has-been-ongoing-for-several-hours. After sunrise, the-onset-of-daytime heating gradually disrupts the stable boundary layer, reducing the conditions favorable for occurrences of-LLJ formation. Consequently, LLJs are less frequent between noon and sunset.

Figure 4(b) shows that, more than 70% of LLJs commonly occur at heights ranging from 0.3 km

332 to 0.8 km AGL in all seasons except summer. The vertical distribution ~~of LLJs occurrences frequency in~~
333 ~~this study also corresponds to agrees with~~ previous studies. For ~~example instance~~, Yan et al. (2021) ~~found~~
334 ~~reported~~ that 400 m AGL was the most frequent height for the jet-nose appearing in the Huaihe River
335 Basin. Wei et al. (2013) revealed that 76% of the observed LLJs ~~were found occurred to occur~~ at an
336 average altitude below 600 m in the Yangtze River Delta region. Following the classification of (Rife et
337 al., (2010), the dominant type of LLJs in Hefei can be identified as BLJs that occur mainly in the PBL
338 below 1 km AGL. The highest occurrence frequency of LLJs appeared between 0.5 km and 0.6 km AGL
339 in ~~all most~~ months, ~~other than July~~, with peak heights between 0.7 and 0.8 km AGL ~~in July~~.

340 The frequent occurrence of LLJs at heights below 1 km AGL enhances vertical mixing and
341 turbulence within the lower atmosphere, breaking the decoupled boundary layer structure and restoring
342 vertical heat, momentum, and pollutant exchanges. During nighttime, when stable stratification
343 dominates, LLJs can reduce the accumulation of air pollutants near the surface by transporting them to
344 higher altitudes. This mechanism is particularly important for urban areas like Hefei, where industrial
345 and vehicular emissions often lead to air quality concerns. The temporal and vertical distribution of LLJs
346 also has practical implications for low-altitude economic activities. For example, understanding LLJ
347 dynamics provides valuable insights for designing safe and efficient drone flight routes, especially in
348 areas with complex terrain or during nighttime operations. Additionally, the strong wind velocities
349 associated with LLJs make them a key consideration for wind energy planning, particularly in optimizing
350 the placement of wind turbines to maximize energy capture and efficiency.

351 ~~The frequency of LLJs occurrences varies with months and heights in Hefei. LLJs occurrences are~~
352 ~~most frequent during spring months, with decreasing frequency from March to May. Our results are~~
353 ~~consistent with Yan et al. (2021), who found that LLJs were the most frequent in spring in Huaihe River~~
354 ~~Basin based on long-term radiosonde observations from 2011 to 2017. The driving mechanisms driving~~
355 ~~to LLJs include inertial oscillations under stable stratification, fronts and baroclinic weather patterns in~~
356 flat terrain, orographic and thermal effects in complex terrain. Considering the topography and weather
357 patterns, Hefei is prone to cyclones throughout the year, so the Asian monsoon system and synoptic
358 processes may be the most important influential factors in LLJs activities. In contrast, previous studies
359 on the LLJ climatology over other typical regions or cities showed different seasonal variations of LLJs
360 occurrences. For example, LLJs occur more often in spring and winter in Beijing while those appear
361 more frequently from October to December and from February to April in Guangzhou using long-term
362 wind profiler observations (Miao et al., 2018).

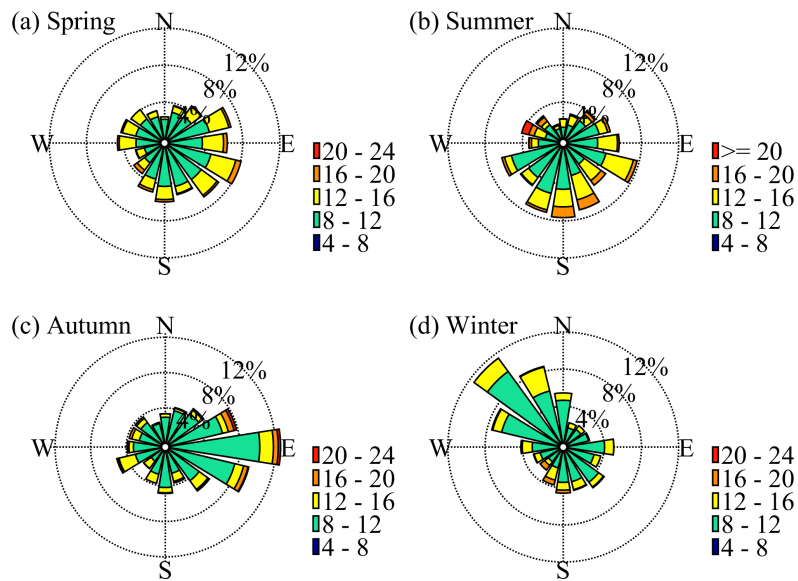


Figure 5. Seasonal wind rose diagrams charts for total of LLJ events at nose height accounted for each season at Hefei. (a) Spring: Mar-May; (b) Summer: Jun-Aug; (c) Autumn: Sep-Nov; and (d) Winter: Dec-Feb.

Figure 5 shows the wind characteristics at the nose height of LLJs across different seasons. The dominant wind directions are southeast in spring, south in summer, and more concentrated in autumn (easterly) and winter (northwesterly). These characteristics in Hefei are closely related to the East Asian monsoon system and associated large-scale atmospheric circulations. In spring, LLJs occur most frequently due to the interaction between cold northerly air masses and warm, moist southerly flows during the transition from the East Asian Winter Monsoon (EAWM) to the East Asian Summer Monsoon (EASM). This dynamic interaction generates strong baroclinic conditions that are favorable for LLJ formation. In summer, the fully developed EASM and the northwestward expansion of the Western Pacific Subtropical High (WPSH) (Wang et al., 2023; Yang et al., 2022) stabilize the boundary layer structure, leading to fewer LLJs compared to spring but with greater intensity (more than half of HWS exceeding 12 m s^{-1}). The predominant wind directions during summer are southerly or southeasterly, reflecting the influence of the monsoonal flow. During autumn and winter, LLJs are less frequent as the WPSH retreats and the EAWM becomes dominant. Autumn marks the gradual transition, with occasional easterly LLJs influenced by the lingering WPSH. In winter, the stable conditions induced by the EAWM and associated high-pressure systems suppress LLJ formation, resulting in weak and infrequent northwesterly LLJs.

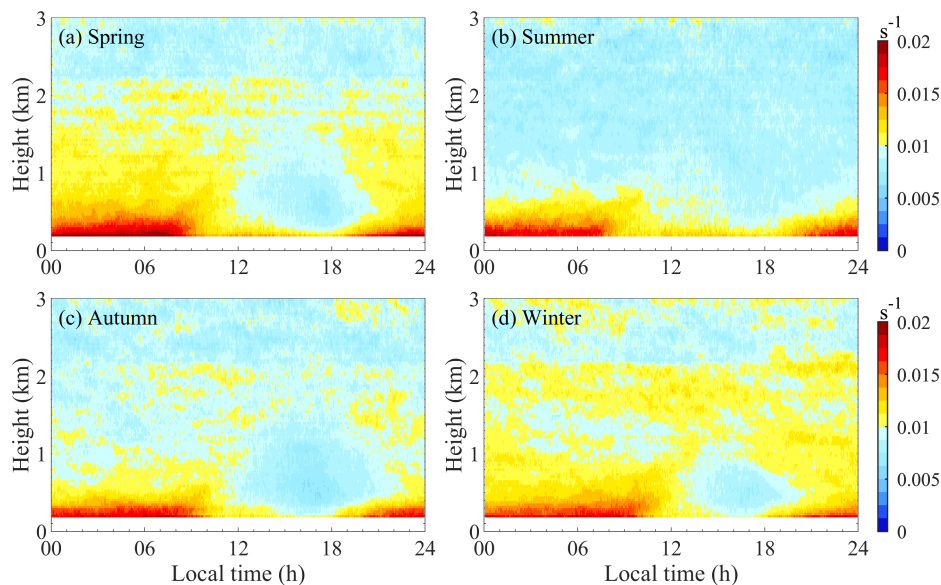
Figure 5(a) shows that the dominant wind directions of LLJs during spring are from the east (E) to the southeast (SE). Furthermore, the maximum HWS of LLJs reaches up to 20 m s^{-1} with more than half of HWS exceeding 12 m s^{-1} . The varying dominant wind directions are associated with the transition from the influence of the East Asian winter monsoon (EAWM) to its summer phase over Hefei. LLJs occurrences peak in March due to its unique atmospheric conditions. During this time, the influence of the winter monsoon is waning, but the full onset of the summer monsoon has not yet occurred. This environment of a mix of cold and warm air masses is particularly favorable for LLJs formation. Compared to March, LLJs occurrences are less frequent in April and May as the East Asian Summer Monsoon (EASM) begins to take hold. As spring progresses, the strong baroclinic conditions that favors LLJs formation begin to weaken. Because the temperature gradient between the cold north and the warming south decreases driven by the growing influence of the western Pacific Subtropical High

393 (WPSH).

394 The overall occurrence frequency of LLJs during summer is lower than that in spring, but their
395 intensity is the strongest. In Figure 5(b), the predominant wind directions of LLJs are from the south (S)
396 and the east southeast (ESE) with peak HWS reaching 20 m s^{-1} . During summer, the fully established
397 EASM is favorable for LLJs formation. Furthermore, the WPSH system extends northwestward from the
398 western Pacific Ocean towards eastern China, stabilizing the atmospheric conditions that favors LLJs
399 formation. The stronger the WPSH, the more intense the pressure gradient, which can lead to stronger
400 southeast-west winds at low levels. The LLJs occurrence generally peak in July, followed by June and
401 August. In July, the EASM is typically at the peak and the WPSH is usually at its most expansive and
402 positioned to exert the strongest influence over eastern China, including Hefei.

403 LLJs occurrences are less frequent during autumn and winter compared to spring and summer.
404 Figure 5(c) shows the predominant easterly wind direction ($>12\%$) of LLJs throughout all autumn months,
405 with the maximum HWS reaching up to 24 m s^{-1} . As autumn approaches, the EASM transitions to the
406 EAWN and the WPSH further shifts eastward and southward (Figure A1). This shift exerts a weaker but
407 persistent influence that channels the air from the east. The least frequency of LLJs occurrences in winter
408 could be associated with general calm wind conditions in the lower troposphere (Figure 3d) and large-
409 scale synoptic systems, like cold fronts and high pressure systems. These systems may not be conducive
410 to the formation of LLJs which typically require a specific set of atmospheric conditions, such as stable
411 conditions and wind shear. During winter, the predominant wind direction of LLJs during winter was
412 from the northwest (NE) in Figure 5(d), which is due to the dominance of the EAWN. The prevailing NE
413 wind of LLJs in winter was not as strong as in the other seasons, with maximum HWS reaching 16 m s^{-1} .
414 Therefore, LLJs in Hefei are dominated by southwesterly winds in summer and northeasterly winds in
415 winter.

416 3.4 Diurnal cycle of VWSH profiles for each season



417
418 **Figure 6.** The same as in Fig. 3 but for VWSH.

419 VWSH depends directly on vertical wind profiles and exhibits both diurnal and seasonal variations
420 within the boundary layer, as shown in Figure 6(a)~(d). Due to surface friction, the wind speeds decrease
421 within the urban canopy, eventually reaching zero at ground level. These rapid changes in wind speed

422 create a large wind speed gradient, resulting in an increased shear intensity in the surface layer.
423 Throughout all seasons in Hefei, high VWSH values exceeding 0.015 m s^{-1} per meter (hereafter denoted
424 by s^{-1}) are typically observed below 0.4 km.

425 Below 0.5 km, VWSH decreases from sunrise to the afternoon due to surface heating and increased
426 atmospheric mixing, which consequently led to a more uniform wind profile (Figure 3). In contrast, it
427 increases from sunset to early morning as surface cooling induces a temperature inversion, which creates
428 a stable boundary layer where winds aloft decouple from the surface. At night, a sharper wind speed
429 gradient with height is created under fully developed stable boundary layer, leading to maximum VWSH
430 in this layer. In the low to mid-level atmosphere (0.5~1 km), VWSH also varies diurnally, with relatively
431 lower values compared to VWSH below 0.5 km. Daytime VWSH in this layer is generally due to the
432 well-mixed boundary layer. But it can vary depending on local weather conditions and synoptic
433 influences. At night, high VWSH values above 0.01 s^{-1} is usually associated with the presence of a LLJ
434 and/or a strong temperature inversion, with the maximum VWSH typically occurring just below the core
435 of the LLJ. In the upper level ($> 1 \text{ km}$), VWSH is less influenced by the diurnal cycle and remained
436 relatively stable throughout the day. However, high VWSH can still occur in this layer when it is coupled
437 with LLJs or influenced by large-scale synoptic systems.

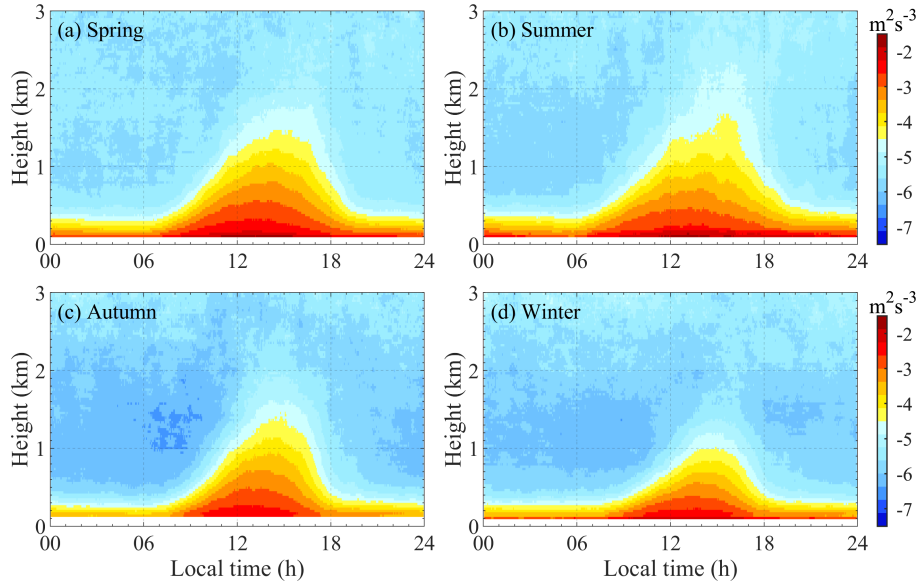
438 The seasonal variation of VWSH is closely linked to the region's climatic patterns, particularly the
439 influence of the East Asian monsoons, which drive significant changes in temperature, wind patterns,
440 and atmospheric stability throughout the year. In general, high VWSH values ($> 0.015 \text{ s}^{-1}$) near the
441 surface are related to LLJs occurrences across all seasons. On the contrary, VWSH values above 1 km in
442 spring and winter are significantly larger compared to summer and autumn, which spatial pattern also
443 corresponds to vertical distributions of seasonal HWS profiles. During the two seasons, Hefei often
444 receives invasion of cold air/surge events, leading to strong winds. In winter, Hefei experiences strong
445 VWSH primarily due to the impact of the EAWM and large-scale synoptic systems, such as cold fronts
446 and jet-streams. Weaker solar heating in winter results in less pronounced diurnal variation of VWSH.
447 These synoptic systems also lead to significant VWSH ($> 0.01 \text{ s}^{-1}$) above 1 km, which is characterized
448 by strong winds aloft. In spring, Hefei experiences strong VWSH due to the transitional atmospheric
449 conditions of the season. The diurnal variation shows a decrease in VWSH after 8:00 a.m. in the morning
450 compared to winter (Figure 6a). The variability in wind directions and speeds contributed to fluctuating
451 VWSH above 1 km influenced by shifting synoptic-scale systems and developing convective activity in
452 late spring.

453 In contrast, relatively lower VWSH values between 0.005 s^{-1} and 0.01 s^{-1} above 1 km are observed
454 in summer. The weather is dominated by the summer monsoon flow and localized convective systems.
455 These conditions result in a generally weaker VWSH with less pronounced diurnal variation compared
456 to other seasons. Due to significant vertical convective mixing, the wind profile becomes more uniform,
457 resulting in weaker VWSH above 1 km (Figure 6b). As the influence of the winter monsoon begins to
458 dominate, the strong winds aloft and weak surface winds contribute to an increasing VWSH in autumn
459 compared to summer (Figure 6c). Similar to winter, VWSH in autumn is more pronounced at night and
460 early morning due to the formation of temperature inversions. During the day, the reduction in VWSH
461 driven by vertical mixing is less noticeable than in summer, as the overall atmospheric stability increases.

462 **3.5 Seasonal characteristics of the diurnal TKEDR profiles**

463 As one of the characteristic features of atmospheric turbulence, the TKEDR plays a crucial role in
464 boundary layer parameterization schemes. It determines the rate at which turbulent kinetic energy is

465 converted into thermal energy, directly influencing the vertical fluxes of momentum, heat, and mass.
466 Long-term measurements of TKEDR will enhance our understanding of boundary layer dynamic
467 processes and lead to more accurate simulations in atmospheric models.



468

469

Figure 7. The same as Fig. 3 but for TKEDR.

470

471

472

473

474

475

476

477

478

479

480

481

482

483

484

485

486

487

488

489

490

491

492

493

494

Figure 7 illustrates the typical diurnal and seasonal cycles of the TKEDR profile. The TKEDR is highest near the surface, with typical values ranging from approximately 10^{-3} to $10^{-2} \text{ m}^2\text{s}^{-3}$, depending on the time of day and season. It decreases with height due to the diminishing influence of surface friction and thermal stratification. The convective boundary layer (or mixing layer) is clearly visible by noting where TKEDR is high. Diurnal variation starts from sunrise, as the increased temperature gradient between the surface and the above air enhances thermal buoyancy, which in turn promotes vertical convective mixing and turbulence. This causes TKEDR near the surface to grow and extend toward higher altitudes. In spring and summer, stronger and longer solar radiation leads to a more developed convective boundary layer, both in terms of duration and height, compared to autumn and winter. The convective boundary layer reaches its peak in the early afternoon, then begins to decay after 16:00 p.m., eventually returning to a shallow well-mixed layer near the ground, approximately 350 m in spring and summer, and around 250 m in autumn and winter. During the night, a stable atmospheric layer was formed near the surface and turbulence was primarily driven by mechanical factors (e.g., wind shear) rather than thermal convection. The complex urban surface roughness enhances wind friction, resulting in intensified turbulence, particularly during spring and summer when nocturnal LLJs occur more frequently. This increased turbulence contributes to the elevated TKEDR observed at night during these seasons.

As TKEDR decreases with altitude, its contour lines (though not explicitly plotted but evident from the color gradations in Figure 7) display a right-skewed shape, with a delayed peak time. This delay can be attributed to two factors: first, convective mixing activity takes time to propagate upward from the surface. Second, the ground cools more rapidly than the air in the late afternoon. Consequently, turbulence at higher altitudes lags low-level activity, reflecting the thermal-driven development of turbulence and energy within the atmospheric boundary layer.

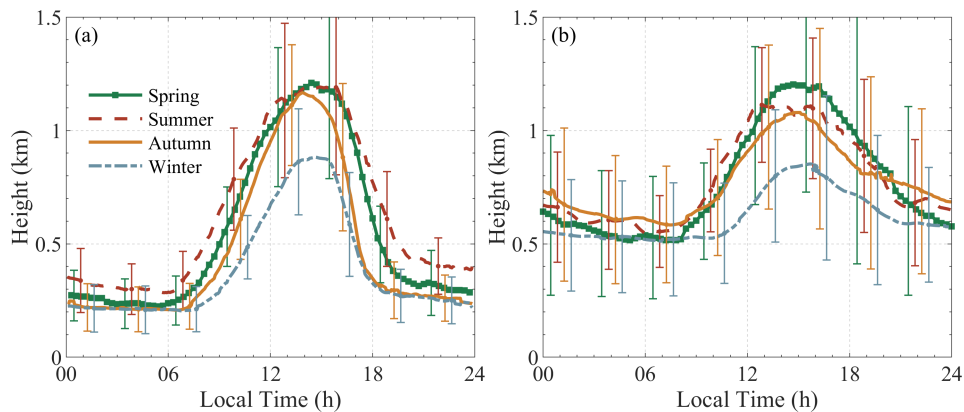
Here, we define the top of the convective boundary layer as the height where TKEDR reaches $10^{-4} \text{ m}^2\text{s}^{-3}$. It should be noted that this height can be different from the MLH given in the next section (Sect.

495 3.6), where the seasonal average MLH is calculated from the daily MLHs. We can see that the top of the
 496 convective boundary layer during daytime in summer exhibits dramatic fluctuations, as shown in Figure
 497 7(b), which could be attributed to the deep convective activities in the afternoon. Unstable atmospheric
 498 stratification enhances vertical convection, leading to the formation of local convective clouds and
 499 thunderstorms. These clouds reduce the amount of solar radiation reaching the surface, causing localized
 500 cooling. Additionally, this process exacerbates the unevenness in the horizontal distribution of
 501 temperature in the affected areas.

502 Overall, these seasonal and diurnal variations in TKEDR highlight the complex interactions
 503 between surface properties, atmospheric stability, and weather systems in shaping the turbulence
 504 characteristics within the boundary layer.

505 3.6 Seasonal variation of diurnal MLH for clear and cloudy days

506 The diurnal variations of MLH and BLH across different seasons in Hefei are depicted in Figure
 507 8(a) and (b), respectively. The MLH is based on turbulence activities, while the BLH is based on the
 508 vertical distribution of material (here aerosol). Therefore, both reflect the diurnal cycle of atmospheric
 509 boundary layer dynamics, but there are some differences.



510
 511 **Figure 8.** Time series plots of the seasonal average (a) MLH and (b) BLH at Hefei. The error bars represent one
 512 standard deviation $\pm\sigma$, and their positions (corresponding to time) vary slightly in different seasons to facilitate
 513 comparison.

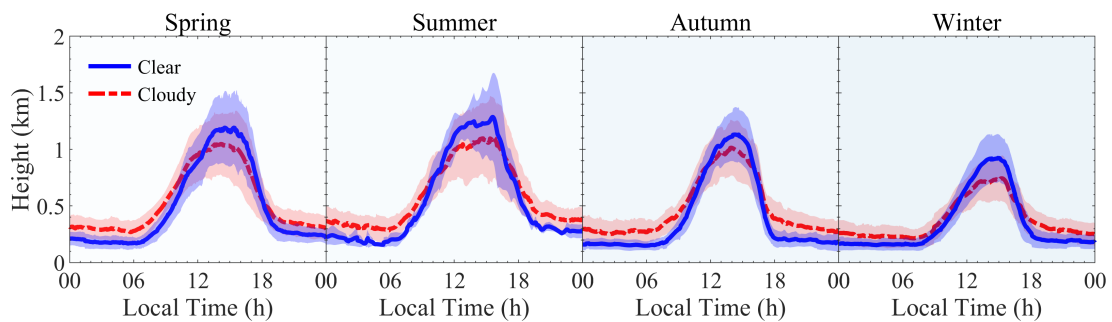
514 After sunrise, surface heating induced by solar radiation promotes the ~~development~~ development of
 515 vertical convective ~~mixing, and mixing and~~ drives the surface aerosols upward. When the temperature
 516 gradient between the surface and air reaches its maximum, the MLH rises fastest, which appears at about
 517 9:00-10:00 a.m. This time varies with seasons, just as the sunrise time, with the earliest in summer,
 518 followed by spring, autumn, and winter. The value of MLH at a certain time also shows the same seasonal
 519 relationship, except for the afternoon in summer. Although solar radiation is highest at noon, the short-
 520 wave incident radiation received by the surface in the afternoon is still greater than the long-wave
 521 outgoing radiation. Therefore, the MLH continues to grow, reaching its maximum between 2:00 p.m. and
 522 3:00 p.m. with about 1.2 km in spring and summer, slightly lower in autumn, and 0.8 km in winter.

523 The similar afternoon peak of MLH between summer and spring could be attributed to several
 524 factors. In the northern hemisphere, the summer solstice which occurs around June 21st or 22nd, is
 525 relatively close to the spring period. This timing means that the transition from spring to summer is not
 526 always abrupt. Furthermore, high surface temperatures and increased evapotranspiration during summer
 527 lead to frequent convective clouds and precipitation. These factors reduce solar radiation received by the

528 ground and weaken convective mixing, which can suppress the MLH. As a result, the seasonally
529 ~~averaged~~ MLH reflects these cloudy conditions, leading to a peak height that may not be as high
530 as one might expect on clear days.

531 In the late afternoon, as surface temperatures decrease due to radiative cooling, vertical convection
532 weakens and turbulence kinetic energy dissipates more rapidly, leading to a faster decline in MLH
533 compared to its increase in the morning. Meanwhile, the decrease in BLH is more gradual due to the
534 slower rate of dry deposition of aerosols. It is noteworthy that the BLH curves exhibit larger fluctuations
535 and significantly higher standard deviations compared to the MLH curves. This is primarily due to the
536 considerable retrieval uncertainty in BLH measurements, which are influenced by aerosol distribution.
537 Transboundary aerosols, clouds, and multilayer aerosols (e.g., residual layer) frequently affect these
538 measurements, a well-recognized issue with aerosol-based BLH retrieval methods (Dang et al., 2019;
539 Mei et al., 2022; Kotthaus et al., 2023; Barlow et al., 2011).

540 During the night, the temperature inversion layer inhibits vertical thermal convection and mixing.
541 Instead, mechanical mixing driven by wind shear becomes predominant, especially in the presence of
542 low-level jets. Consequently, the MLH is typically highest in summer at about 0.3 km, followed by spring,
543 and lowest in autumn and winter, about 0.2 km. In contrast, The BLH remains higher than the MLH, at
544 approximately 0.5~0.7 km. The higher nocturnal BLH in autumn may be related to the transboundary
545 transport of aerosols and meteorological factors. Both the MLH and the BLH continue to decrease and
546 reach their minimum at sunrise in the next diurnal cycle.



547

548 **Figure 9.** Time series plots of the seasonal average MLH (lines) and one-sigma standard deviation (shaded areas)
549 for clear days and cloudy days during each season at Hefei, respectively.

550 To further investigate the influence of clouds on the development of MLH, we compared the
551 seasonally averaged diurnal MLH under different weather conditions, as shown in Figure 9. The diurnal
552 MLH showed significant differences between clear and cloudy days and exhibited similar characteristics
553 in each season. Overall, the diurnal variation of the MLH was less pronounced on cloudy days with
554 a flatter curve, due to the modulation of clouds on the surface radiation budget. During daytime, the
555 presence of clouds typically reduces surface heating by solar radiation, which inhibits the development
556 of vertical convective mixing and results in a shallower mixed layer compared to clear weather conditions.
557 The difference of MLH reaches its maximum of about 200 m in the afternoon. While during the night,
558 clouds act as a "greenhouse" by absorbing longwave radiation from the ground and slowing down the
559 radiative cooling, which results in a higher MLH compared to clear days. The mean difference in MLH
560 between cloudy and clear days is about 100 m.

561 Note that, the diurnal MLH in summer showed relatively large variations, particularly on clear days.
562 This variability can be attributed to strong and variable convective activity, as well as to the limited
563 number of data samples. Plum rains and frequent convective clouds in summer lead to a much lower

564 proportion of sunny days than in other seasons.

565 **4. Conclusions Summary and Conclusions discussion**

566 ~~In this study, three years of Doppler wind lidar measurements (spanning from June 2019~~
567 ~~to June 2022) were utilized to characterize the PBL dynamics over Hefei, a rapidly developing city~~
568 ~~in the western YRD, China. Compared to aerosol lidars, the CDWL is capable of providing additional~~
569 ~~Doppler information including vertical wind profiles, wind shear~~
570 ~~intensity, low-level jets, and turbulence mixing, and boundary layer height, with high spatiotemporal~~
571 ~~resolution. This study provides a detailed characterization of the seasonal and diurnal variability of urban~~
572 ~~PBL dynamics in a monsoon-influenced subtropical environment.~~

573 ~~The results showed that HWS steady increase from 2 to 7 m s⁻¹ between 300 m and 3 km AGL, with~~
574 ~~a more rapid acceleration above 3 km, particularly in autumn and winter. Westerly winds (270°±15°)~~
575 ~~dominated above 3 km, while wind directions within the PBL were more variable, influenced by local~~
576 ~~topography and surface roughness. LLJs primarily formed at sunset and dissipated by noon, typically~~
577 ~~occurring at altitudes between 0.5 and 0.6 km throughout the year, except in July. LLJ occurrences were~~
578 ~~most frequent in spring (31.7%), followed by summer (24.7%), autumn (22.3%), and winter (21.3%),~~
579 ~~with the strongest LLJs observed in summer, extending up to 1.5 km.~~

580 ~~Strong wind speed gradients below and above the LLJs induced large VWSH vertical wind shear~~
581 ~~intensity (up to 0.02 s⁻¹) and elevated TKEDR (up to 10⁻³² m²s⁻³) in the near-surface layer at night,~~
582 ~~promoting vertical mixing of pollutants.~~

583 ~~Seasonal wind direction shifts of LLJ nose (e.g., southerly in summer and northeasterly in winter)~~
584 ~~reflected the interplay between monsoonal flows and local topography. During the daytime, TKEDR~~
585 ~~increased and extend toward higher altitudes with the transport of heat, momentum and TKEDR was~~
586 ~~generally highest near the surface, ranging from 10⁻³ to 10⁻² m²s⁻³ in all seasons. mass. Turbulence mixing~~
587 ~~slowed down wind speeds by increasing surface friction, forming a gentler wind zone and reducing shear~~
588 ~~intensity. An interesting fluctuation in TKEDR above the MLH top during early summer afternoons was~~
589 ~~attributed to atmospheric instability after continuous surface heating.~~

590 ~~The dynamics-based MLH BLH exhibited smaller larger fluctuations and lower and greater standard~~
591 ~~deviations compared to the aerosol-based BLH-MLH. The peak-MLH peaked occurred between 2:00~~
592 ~~p.m. and 3:00 p.m., reaching ~1.2 km in spring and summer, slightly lower in autumn, and around 0.8~~
593 ~~km in winter. After sunset, it eventually returned to a shallow well-mixed layer near the ground (~350 m~~
594 ~~in spring and summer, and ~250 m in autumn and winter). Compared to clear days, cloud cover reduces~~
595 ~~the MLH by about 200 m at the afternoon peak time, while increasing it by approximately 100 m at night.~~
596 ~~These results quantified the different influence of cloud coverage to the development of MLH during day~~
597 ~~and night.~~

598 ~~In conclusion, this study leverages the high temporal and spatial resolution of Doppler wind lidar to~~
599 ~~provide a detailed characterization of urban PBL dynamics, offering valuable insights into their complex~~
600 ~~interactions with surface heating and cooling, atmospheric stability, cloud, and synoptic-scale weather~~
601 ~~systems. Long-term lidar observations of LLJs, MLH, and TKEDR provide critical insights into vertical~~
602 ~~mixing, turbulence, and pollutant transport in a monsoon-influenced subtropical environment, enriching~~
603 ~~the climatological understanding of LLJs and PBL processes over the western Yangtze River Delta. These~~
604 ~~results have also significant practical implications, serving as valuable references for local standards and~~
605 ~~regional planning by supporting strategies for urban air quality management and the development of low-~~
606 ~~altitude economic activities. Specifically, the results inform vertical zoning for applications such as wind~~

607 energy development and drone logistics, guiding optimal turbine placement and flight route planning.
608 Overall, this study underscores the importance of lidar-based observations in addressing regional
609 atmospheric challenges and advancing environmental and economic sustainability.

610 Despite these insights, this study is constrained to a single urban observational site and focuses on
611 statistical analysis. Future research will extend observations to multiple sites, including urban, suburban,
612 and rural to comprehensively capture the spatial variability of PBL processes and LLJ characteristics
613 across different land-use types and topographic conditions. Additionally, subsequent studies will conduct
614 specific case analyses under varying meteorological scenarios, integrating aerosol observations and high-
615 resolution numerical models. These efforts aim to enhance our understanding of the interactions between
616 aerosols, clouds, radiation, and PBL dynamics, particularly their influence on vertical mixing and
617 boundary layer evolution.

618 ~~Moreover, we identified LLJs events based on the nose characteristic of wind speed and retrieved both~~
619 ~~the turbulence-based MLH and the aerosol-based BLH. Both seasonal and diurnal variations of these key~~
620 ~~parameters were comprehensively analyzed to shed new insights into the structure and dynamics of the~~
621 ~~PBL. The results are summarized as follows:~~

622 ~~(1) Seasonal characteristics of wind profile: The frequency distribution of HWS exhibited a~~
623 ~~rightward skew in all seasons, with lower values near the ground, and with a steady increase from 2 to 7~~
624 ~~m s^{-1} between 300 m and 3 km AGL, and a more rapid acceleration above 3 km. HWS% profiles in spring~~
625 ~~and summer were more dispersed, with a lower frequency of high HWS occurrences ($\text{HWS} > 10 \text{ m s}^{-1}$)~~
626 ~~above 3 km. Seasonal HWD% profiles showed a predominance of westerly winds ($270^\circ \pm 15^\circ$) above 3~~
627 ~~km, while HWD within the PBL was more variable and chaotic. Seasonal VWS% profiles also exhibited~~
628 ~~a right-skewed pattern with central values ranging between -0.2 m s^{-1} and -0.1 m s^{-1} , indicating upward~~
629 ~~motion. Winter, influenced by cold fronts associated with the winter monsoon, had the highest frequency~~
630 ~~of negative VWS values, ranging from 4% to 7% below 3 km AGL.~~

631 ~~(2) Diurnal characteristics of wind profile: A typical GWZ ($\text{HWS} < 5 \text{ m s}^{-1}$) formed in the PBL~~
632 ~~during the day in all seasons, with its diurnal variation strongly correlated with the development of the~~
633 ~~mixing layer. The vertical height of high wind zone ($> 8 \text{ m s}^{-1}$) during the day was much lower than at~~
634 ~~night, particularly in winter, reaching 1.5 km between 11:00 a.m. and 4:00 p.m. In all seasons except~~
635 ~~winter, a distinct local maximum in HWS between 0.4 km and 0.8 km was observed after 8:00 p.m. and~~
636 ~~before 7:00 a.m. the next day. The phenomenon was most pronounced in summer due to the influence of~~
637 ~~nocturnal LLJs.~~

638 ~~(3) Monthly characteristics of LLJs: The dominant type was identified as BLJs in Hefei, with~~
639 ~~occurrences being most frequent in spring (31.7%), followed by summer (24.7%), autumn (22.3%), and~~
640 ~~winter (21.3%) in. LLJs were more frequently during the night and early morning throughout the year,~~
641 ~~with 70% typically occurring at heights ranging from 0.3 km to 0.8 km AGL in all seasons except summer.~~
642 ~~The highest occurrence frequency of LLJs appeared between 0.5 km and 0.6 km AGL in all months other~~
643 ~~than July, with peak heights between 0.7 and 0.8 km AGL. Predominant wind directions of LLJs were~~
644 ~~from the E and SE in spring, from S and ESE in summer, from E in autumn, and from NE in winter. LLJs~~
645 ~~in summer were most intensified with largest frequency of high HWS ($> 16 \text{ m s}^{-1}$) and extended to~~
646 ~~altitudes of up to 1.5 km.~~

647 ~~(4) Seasonal and diurnal characteristics of VWSH, TKEDR, and BLH: High VWSH values~~
648 ~~exceeding 0.015 s^{-1} were typically observed below 0.4 km, which was usually associated with the LLJs~~
649 ~~and/or strong temperature inversions at night. VWSH values above 1 km were significantly larger in~~
650 ~~spring and winter compared to summer and autumn, correlating with vertical distributions of seasonal~~

651 **HWS profiles.** Strong wind speed gradients below and above the LLJs induced large vertical wind shear
652 intensity (up to 0.02 s^{-1}) and TKEDR (up to $10^{-3}\text{ m}^2\text{ s}^{-2}$) in the near-surface layer at night. TKEDR was
653 generally highest near the surface, ranging from 10^{-3} to $10^{-2}\text{ m}^2\text{ s}^{-2}$ in all seasons. The BLH exhibited larger
654 fluctuations and greater standard deviations compared to the MLH. The peak MLH occurred between
655 2:00 p.m. and 3:00 p.m., reaching 1.2 km in spring and summer, slightly lower in autumn, and around
656 0.8 km in winter. After sunset, it eventually returned to a shallow well-mixed layer near the ground (~350
657 m in spring and summer, and ~250 m in autumn and winter). Compared to clear days, cloud cover reduces
658 the MLH by about 200 m at the afternoon peak time, while increasing it by approximately 100 m at night.

659 **In conclusion,** these analyses highlight the characteristics of PBL dynamics and their complex
660 interactions with surface heating/cooling, atmospheric stability, and synoptic-scale weather patterns. The
661 long-term statistical results will not only advance scientific understanding, but will also serve as essential
662 references for formulating local standards and regional delineation, including vertical zoning, related to
663 low-altitude economic activities, such as wind energy and drone logistics.

664
665
666 **Data Availability.** The Doppler wind lidar data used in this study can be provided for non-commercial
667 research purposes upon request to the first author (Tianwen Wei: twwei@nuist.edu.cn). **The ERA5 data**
668 **sets are publicly available from the ECMWF website at <https://eds.climate.ecmwf.eu>.**

669
670 **Author contributions.** Tianwen Wei: Conceptualization, Methodology, Data curation, Formal analysis,
671 Visualization, Writing – review & editing. Mengya Wang: Conceptualization, Writing – original draft,
672 Methodology, Investigation. Kenan Wu: Resources, Data curation. Jinlong Yuan: Resources, Data
673 curation. Haiyun Xia: Conceptualization, Supervision, Resources, Validation. Simone Lolli: Writing –
674 review & editing, Validation.

675
676 **Conflict of Interest.** Some authors are members of the editorial board of Atmospheric Measurement
677 Techniques.

678
679 **Financial support.** This work was supported by the National Natural Science Foundation of China
680 (42405136), [the China Meteorological Administration Xiong'an Atmospheric Boundary Layer Key](#)
681 [Laboratory \(2023LABL-B11\)](#), the Natural Science Research of Jiangsu Higher Education Institutions of
682 China (23KJB170012).

684 Reference

- 685 Baklanov, A. A., Grisogono, B., Bornstein, R., Mahrt, L., Zilitinkevich, S. S., Taylor, P., Larsen, S. E., Rotach, M. W., and Fernando,
686 H. J. S.: The nature, theory, and modeling of atmospheric planetary boundary layers, *Bull. Am. Meteorol. Soc.*, 92, 123–128,
687 <https://doi.org/10.1175/2010BAMS2797.1>, 2011.
- 688 Banakh, V. A., Brewer, A., Pichugina, E. L., and Smalikho, I. N.: Measurements of wind velocity and direction with coherent
689 doppler lidar in conditions of a weak echo signal, *Atmospheric Ocean. Opt.*, 23, 381–388,
690 <https://doi.org/10.1134/S1024856010050076>, 2010.
- 691 Banakh, V. A., Smalikho, I. N., and Falits, A. V.: Estimation of the turbulence energy dissipation rate in the atmospheric boundary
692 layer from measurements of the radial wind velocity by micropulse coherent doppler lidar, *Opt. Express*, 25, 22679,

693 <https://doi.org/10.1364/oe.25.022679>, 2017.

694 Banakh, V. A., Smalikhov, I. N., and Falits, A. V.: Estimation of the height of the turbulent mixing layer from data of doppler lidar
695 measurements using conical scanning by a probe beam, *Atmospheric Meas. Tech.*, 14, 1511–1524,
696 <https://doi.org/10.5194/amt-14-1511-2021>, 2021.

697 Barlow, J. F.: Progress in observing and modelling the urban boundary layer, *Urban Clim.*, 10, 216–240,
698 <https://doi.org/10.1016/j.uclim.2014.03.011>, 2014.

699 Barlow, J. F., Dunbar, T. M., Nemitz, E. G., Wood, C. R., Gallagher, M. W., Davies, F., O’Connor, E., and Harrison, R. M.: Boundary
700 layer dynamics over London, UK, as observed using Doppler lidar during REPARTEE-II, *Atmospheric Chem. Phys.*, 11,
701 2111–2125, <https://doi.org/10.5194/acp-11-2111-2011>, 2011.

702 Blackadar, A. K.: Boundary layer wind maxima and their significance for the growth of nocturnal inversions, *Bull. Am. Meteorol.*
703 *Soc.*, 38, 283–290, <https://doi.org/10.1175/1520-0477-38.5.283>, 1957.

704 Caicedo, V., Rappenglück, B., Lefer, B., Morris, G., Toledo, D., and Delgado, R.: Comparison of aerosol lidar retrieval methods
705 for boundary layer height detection using ceilometer aerosol backscatter data, *Atmospheric Meas. Tech.*, 10, 1609–1622,
706 <https://doi.org/10.5194/amt-10-1609-2017>, 2017.

707 Caughey, S. J. and Palmer, S. G.: Some aspects of turbulence structure through the depth of the convective boundary layer, *Q. J.*
708 *R. Meteorol. Soc.*, 105, 811–827, <https://doi.org/10.1002/qj.49710544606>, 1979.

709 Chen, S., Tong, B., Russell, L. M., Wei, J., Guo, J., Mao, F., Liu, D., Huang, Z., Xie, Y., Qi, B., Zhang, H., Sun, Y., Zhang, B., Xu,
710 C., Wu, L., and Liu, D.: Lidar-based daytime boundary layer height variation and impact on the regional satellite-based PM_{2.5}
711 estimate, *Remote Sens. Environ.*, 281, 113224, <https://doi.org/10.1016/j.rse.2022.113224>, 2022.

712 Chen, Y., Zhang, A., Zhang, Y., Cui, C., Wan, R., Wang, B., and Fu, Y.: A heavy precipitation event in the Yangtze River basin led
713 by an eastward moving tibetan plateau cloud system in the summer of 2016, *J. Geophys. Res. Atmospheres*, 125,
714 e2020JD032429, <https://doi.org/10.1029/2020JD032429>, 2020.

715 Chen, Y.-C., Xue, L., Lebo, Z. J., Wang, H., Rasmussen, R. M., and Seinfeld, J. H.: A comprehensive numerical study of aerosol-
716 cloud-precipitation interactions in marine stratocumulus, *Atmospheric Chem. Phys.*, 11, 9749–9769,
717 <https://doi.org/10.5194/acp-11-9749-2011>, 2011.

718 Christensen, M. W., Wu, P., Varble, A. C., Xiao, H., and Fast, J. D.: Aerosol-induced closure of marine cloud cells: enhanced effects
719 in the presence of precipitation, *Atmospheric Chem. Phys.*, 24, 6455–6476, <https://doi.org/10.5194/acp-24-6455-2024>, 2024.

720 Cui, C., Zhou, W., Yang, H., Wang, X., Deng, Y., Wang, X., Xu, G., and Wang, J.: Analysis of the characteristics of the low-level
721 jets in the middle reaches of the Yangtze River during the mei-yu season, *Adv. Atmospheric Sci.*, 40, 711–724,
722 <https://doi.org/10.1007/s00376-022-2107-1>, 2023.

723 Dang, R., Yang, Y., Li, H., Hu, X.-M., Wang, Z., Huang, Z., Zhou, T., and Zhang, T.: Atmosphere boundary layer height (ABLH)
724 determination under multiple-layer conditions using micro-pulse lidar, *Remote Sens.*, 11, 263,
725 <https://doi.org/10.3390/rs11030263>, 2019.

726 Du, Y., Zhang, Q., Chen, Y., Zhao, Y., and Wang, X.: Numerical simulations of spatial distributions and diurnal variations of low-
727 level jets in China during early summer, *J. Clim.*, 27, 5747–5767, <https://doi.org/10.1175/JCLI-D-13-00571.1>, 2014.

728 Fochesatto, G. J., Drobinski, P., Flamant, C., Guedalia, D., Sarrat, C., Flamant, P. H., and Pelon, J.: Evidence of dynamical coupling
729 between the residual layer and the developing convective boundary layer, *Bound.-Layer Meteorol.*, 99, 451–464,
730 <https://doi.org/10.1023/A:1018935129006>, 2001.

731 Garratt, J.: Review: the atmospheric boundary layer, *Earth-Sci. Rev.*, 37, 89–134, [https://doi.org/10.1016/0012-8252\(94\)90026-4](https://doi.org/10.1016/0012-8252(94)90026-4),
732 1994.

733 Gu, L., Yao, J., Hu, Z., Ma, Y., Sun, F., Yu, H., Wang, S., Yang, Y., Guo, R., and Qin, Y.: Characteristics of the atmospheric boundary
734 layer’s structure and heating (cooling) rate in summer over the northern Tibetan Plateau, *Atmospheric Res.*, 269, 106045,
735 <https://doi.org/10.1016/j.atmosres.2022.106045>, 2022.

736 Guo, J., Li, Y., Cohen, J. B., Li, J., Chen, D., Xu, H., Liu, L., Yin, J., Hu, K., and Zhai, P.: Shift in the temporal trend of boundary
737 layer height in China using long-term (1979–2016) radiosonde data, *Geophys. Res. Lett.*, 46, 6080–6089,
738 <https://doi.org/10.1029/2019GL082666>, 2019.

739 Guo, J., Zhang, J., Yang, K., Liao, H., Zhang, S., Huang, K., Lv, Y., Shao, J., Yu, T., Tong, B., Li, J., Su, T., Yim, S. H. L., Stoffelen,
740 A., Zhai, P., and Xu, X.: Investigation of near-global daytime boundary layer height using high-resolution radiosondes: first
741 results and comparison with ERA5, MERRA-2, JRA-55, and NCEP-2 reanalyses, *Atmospheric Chem. Phys.*, 21, 17079–
742 17097, <https://doi.org/10.5194/acp-21-17079-2021>, 2021.

743 Hu, F., Xie, P., Xu, J., Li, A., Lv, Y., Zhang, Z., Zheng, J., and Tian, X.: Impacts of synoptic weather patterns on hefei’s ozone in
744 warm season and analysis of transport pathways during extreme pollution events, *J. Environ. Sci.*,
745 <https://doi.org/10.1016/j.jes.2024.06.032>, 2024.

746 Huang, M., Gao, Z., Miao, S., Chen, F., LeMone, M. A., Li, J., Hu, F., and Wang, L.: Estimate of boundary-layer depth over beijing,
747 china, using doppler lidar data during SURF-2015, *Bound.-Layer Meteorol.*, 162, 503–522, <https://doi.org/10.1007/s10546-016-0205-2>, 2017.

748
749 Jia, M., Yuan, J., Wang, C., Xia, H., Wu, Y., Zhao, L., Wei, T., Wu, J., Wang, L., Gu, S. Y., Liu, L., Lu, D., Chen, R., Xue, X., and
750 Dou, X.: Long-lived high-frequency gravity waves in the atmospheric boundary layer: Observations and simulations,

751 Atmospheric Chem. Phys., 19, 15431–15446, <https://doi.org/10.5194/acp-19-15431-2019>, 2019.

752 Jiang, P., Yuan, J., Wu, K., Wang, L., and Xia, H.: Turbulence detection in the atmospheric boundary layer using coherent doppler
753 wind lidar and microwave radiometer, *Remote Sens.*, 14, 2951, <https://doi.org/10.3390/rs14122951>, 2022.

754 Justus, C. G., Hargraves, W. R., Mikhail, A., and Graber, D.: Methods for estimating wind speed frequency distributions, *J. Appl.*
755 *Meteorol.*, 17, 350–353, [https://doi.org/10.1175/1520-0450\(1978\)017<0350:MFEWSF>2.0.CO;2](https://doi.org/10.1175/1520-0450(1978)017<0350:MFEWSF>2.0.CO;2), 1978.

756 Kang, H., Zhu, B., Gao, J., He, Y., Wang, H., Su, J., Pan, C., Zhu, T., and Yu, B.: Potential impacts of cold frontal passage on air
757 quality over the Yangtze River delta, china, *Atmospheric Chem. Phys.*, 19, 3673–3685, [https://doi.org/10.5194/acp-19-3673-](https://doi.org/10.5194/acp-19-3673-2019)
758 2019, 2019.

759 Kim, C. P. and Entekhabi, D.: Feedbacks in the land-surface and mixed-layer energy budgets, *Bound.-Layer Meteorol.*, 88, 1–21,
760 <https://doi.org/10.1023/A:1001094008513>, 1998.

761 Kotthaus, S., Bravo-Aranda, J. A., Collaud Coen, M., Guerrero-Rascado, J. L., Costa, M. J., Cimini, D., O’Connor, E. J., Hervo,
762 M., Alados-Arboledas, L., Jiménez-Portaz, M., Mona, L., Ruffieux, D., Illingworth, A., and Haefelin, M.: Atmospheric
763 boundary layer height from ground-based remote sensing: a review of capabilities and limitations, *Atmospheric Meas. Tech.*,
764 16, 433–479, <https://doi.org/10.5194/amt-16-433-2023>, 2023.

765 Li, C., Li, H., Zhang, Y., Zha, D., Zhao, B., Yang, S., Zhang, B., and De Boer, W. F.: Predicting hydrological impacts of the Yangtze-
766 to-huaihe water diversion project on habitat availability for wintering waterbirds at caizi lake, *J. Environ. Manage.*, 249,
767 109251, <https://doi.org/10.1016/j.jenvman.2019.07.022>, 2019.

768 Li, L., Zhu, A., Huang, L., Wang, Q., Chen, Y., Ooi, M. C. G., Wang, M., Wang, Y., and Chan, A.: Modeling the impacts of land
769 use/land cover change on meteorology and air quality during 2000–2018 in the Yangtze River delta region, china, *Sci. Total*
770 *Environ.*, 829, 154669, <https://doi.org/10.1016/j.scitotenv.2022.154669>, 2022a.

771 Li, L., Wang, Y., Lu, J., Wang, X., Wu, P., and Tao, Y.: Spatial and temporal variability of maximum wind speed and extreme wind
772 speed in Anhui Province during different recurrence intervals from 1981 to 2020, *J. Trop. Meteorol.*, 38, 662–670,
773 <https://doi.org/10.16032/j.issn.1004-4965.2022.060>, 2022b.

774 Li, X., Li, Q.-P., Ding, Y.-H., and Wang, M.: Near-surface wind speed changes in eastern China during 1970–2019 winter and its
775 possible causes, *Adv. Clim. Change Res.*, 13, 228–239, <https://doi.org/10.1016/j.accre.2022.01.003>, 2022c.

776 Li, X.-B., Han, Y.-X., Fu, Z.-Y., Zhang, Y.-C., Fan, M., Sang, S.-J., Chen, X.-X., Liang, B.-Y., Liu, Y.-C., Lu, P.-C., Li, H.-W., Pan,
777 H.-F., and Yang, J.-M.: Association of sudden sensorineural hearing loss with meteorological factors: a time series study in
778 hefei, china, and a literature review, *Environ. Sci. Pollut. Res.*, 31, 42970–42990, [https://doi.org/10.1007/s11356-024-33943-](https://doi.org/10.1007/s11356-024-33943-1)
779 1, 2024.

780 Li, Z., Guo, J., Ding, A., Liao, H., Liu, J., Sun, Y., Wang, T., Xue, H., Zhang, H., and Zhu, B.: Aerosol and boundary-layer
781 interactions and impact on air quality, *Natl. Sci. Rev.*, 4, 810–833, <https://doi.org/10.1093/nsr/nwx117>, 2017.

782 Li, Z., Song, L., Ma, H., Xiao, J., Wang, K., and Chen, L.: Observed surface wind speed declining induced by urbanization in east
783 China, *Clim. Dyn.*, 50, 735–749, <https://doi.org/10.1007/s00382-017-3637-6>, 2018.

784 Liu, H., Huang, X., Fei, J., Zhang, C., and Cheng, X.: Spatiotemporal features and associated synoptic patterns of extremely
785 persistent heavy rainfall over china, *J. Geophys. Res. Atmospheres*, 127, e2022JD036604,
786 <https://doi.org/10.1029/2022JD036604>, 2022.

787 Liu, L., Liang, Y., He, C., Li, B., Chu, L., and Li, J.: Evaluating the contribution of climate change and urbanization to the reversal
788 in maximum surface wind speed decline: case study in the Yangtze River economic belt, china, *Urban Clim.*, 52, 101713,
789 <https://doi.org/10.1016/j.uclim.2023.101713>, 2023.

790 Liu, X., Guo, Q., Guo, Z., Yin, Z.-Y., Dong, B., and Smith, R.: Where were the monsoon regions and arid zones in Asia prior to
791 the Tibetan Plateau uplift?, *Natl. Sci. Rev.*, 2, 403–416, <https://doi.org/10.1093/nsr/nwv068>, 2015.

792 Madala, S., Satyanarayana, A. N. V., and Rao, T. N.: Performance evaluation of PBL and cumulus parameterization schemes of
793 WRF ARW model in simulating severe thunderstorm events over gadanki MST radar facility — case study, *Atmospheric Res.*,
794 139, 1–17, <https://doi.org/10.1016/j.atmosres.2013.12.017>, 2014.

795 Manninen, A. J., Marke, T., Tuononen, M., and O’Connor, E. J.: Atmospheric boundary layer classification with doppler lidar, *J.*
796 *Geophys. Res. Atmospheres*, 123, 8172–8189, <https://doi.org/10.1029/2017JD028169>, 2018.

797 Mei, L., Wang, X., Gong, Z., Liu, K., Hua, D., and Wang, X.: Retrieval of the planetary boundary layer height from lidar
798 measurements by a deep-learning method based on the wavelet covariance transform, *Opt. Express*, 30, 16297,
799 <https://doi.org/10.1364/OE.454094>, 2022.

800 Miao, Y., Guo, J., Liu, S., Wei, W., Zhang, G., Lin, Y., and Zhai, P.: The climatology of low-level jet in beijing and guangzhou,
801 china, *J. Geophys. Res. Atmospheres*, 123, 2816–2830, <https://doi.org/10.1002/2017JD027321>, 2018.

802 Mirza, A. K., Dacre, H. F., and Lo, C. H. B.: A case study analysis of the impact of a new free tropospheric turbulence scheme on
803 the dispersion of an atmospheric tracer, *Q. J. R. Meteorol. Soc.*, 150, 1907–1925, <https://doi.org/10.1002/qj.4681>, 2024.

804 O’Connor, E. J., Illingworth, A. J., Brooks, I. M., Westbrook, C. D., Hogan, R. J., Davies, F., and Brooks, B. J.: A method for
805 estimating the turbulent kinetic energy dissipation rate from a vertically pointing doppler lidar, and independent evaluation
806 from balloon-borne in situ measurements, *J. Atmospheric Ocean. Technol.*, 27, 1652–1664,
807 <https://doi.org/10.1175/2010jtecha1455.1>, 2010.

808 Ortiz-Amezcuca, P., Andújar-Maqueda, J., Manninen, A. J., Pentikäinen, P., O’Connor, E. J., Stachlewska, I. S., De Arruda Moreira,

809 G., Benavent-Oltra, J. A., Casquero-Vera, J. A., Poczta, P., Wang, D., Harenda, K. M., Chojnicki, B. H., Szczepanik, D. M.,
810 Janicka, L., Schüttemeyer, D., Alados-Arboledas, L., and Guerrero-Rascado, J. L.: Dynamics of the atmospheric boundary
811 layer over two middle-latitude rural sites with doppler lidar, *Atmospheric Res.*, 280, 106434,
812 <https://doi.org/10.1016/j.atmosres.2022.106434>, 2022.

813 Parsons, D. B.: An explanation for intense frontal updrafts and narrow cold-frontal rainbands, *J. Atmospheric Sci.*, 49, 1810–1825,
814 [https://doi.org/10.1175/1520-0469\(1992\)049<1810:AEFIFU>2.0.CO;2](https://doi.org/10.1175/1520-0469(1992)049<1810:AEFIFU>2.0.CO;2), 1992.

815 Pérez-Ramírez, D., Whiteman, D. N., Veselovskii, I., Colarco, P., Korenski, M., and da Silva, A.: Retrievals of aerosol single
816 scattering albedo by multiwavelength lidar measurements: Evaluations with NASA langley HSRL-2 during discover-AQ field
817 campaigns, *Remote Sens. Environ.*, 222, 144–164, <https://doi.org/10.1016/j.rse.2018.12.022>, 2019.

818 Pérez-Ramírez, D., Whiteman, D. N., Veselovskii, I., Ferrare, R., Titos, G., Granados-Muñoz, M. J., Sánchez-Hernández, G., and
819 Navas-Guzmán, F.: Spatiotemporal changes in aerosol properties by hygroscopic growth and impacts on radiative forcing and
820 heating rates during DISCOVER-AQ 2011, *Atmospheric Chem. Phys.*, 21, 12021–12048, [https://doi.org/10.5194/acp-21-](https://doi.org/10.5194/acp-21-12021-2021)
821 [12021-2021](https://doi.org/10.5194/acp-21-12021-2021), 2021.

822 Petrosyan, A., Galperin, B., Larsen, S. E., Lewis, S. R., Määttänen, A., Read, P. L., Renno, N., Rogberg, L. P. H. T., Savijärvi, H.,
823 Siili, T., Spiga, A., Toigo, A., and Vázquez, L.: The martian atmospheric boundary layer, *Rev. Geophys.*, 49, 2010RG000351,
824 <https://doi.org/10.1029/2010RG000351>, 2011.

825 Pobočková, I., Sedláčková, Z., and Michalková, M.: Application of four probability distributions for wind speed modeling,
826 *Procedia Eng.*, 192, 713–718, <https://doi.org/10.1016/j.proeng.2017.06.123>, 2017.

827 Qin, R. X., Xiao, C., Zhu, Y., Li, J., Yang, J., Gu, S., Xia, J., Su, B., Liu, Q., and Woodward, A.: The interactive effects between
828 high temperature and air pollution on mortality: a time-series analysis in hefei, china, *Sci. Total Environ.*, 575, 1530–1537,
829 <https://doi.org/10.1016/j.scitotenv.2016.10.033>, 2017.

830 Qiu, Z., Xian, J., Yang, Y., Lu, C., Yang, H., Hu, Y., Sun, J., and Zhang, C.: Characteristics of coastal low-level jets in the boundary
831 layer of the pearl river estuary, *J. Mar. Sci. Eng.*, 11, 1128, <https://doi.org/10.3390/jmse11061128>, 2023.

832 Rife, D. L., Pinto, J. O., Monaghan, A. J., Davis, C. A., and Hannan, J. R.: Global distribution and characteristics of diurnally
833 varying low-level jets, *J. Clim.*, 23, 5041–5064, <https://doi.org/10.1175/2010jcli3514.1>, 2010.

834 Shen, L., Cheng, Y., Bai, X., Dai, H., Wei, X., Sun, L., Yang, Y., Zhang, J., Feng, Y., Li, Y. J., Chen, D.-R., Liu, J., and Gui, H.:
835 Vertical profile of aerosol number size distribution during a haze pollution episode in hefei, china, *Sci. Total Environ.*, 814,
836 152693, <https://doi.org/10.1016/j.scitotenv.2021.152693>, 2022.

837 Shi, C., Roth, M., Zhang, H., and Li, Z.: Impacts of urbanization on long-term fog variation in anhui province, china, *Atmos.*
838 *Environ.*, 42, 8484–8492, <https://doi.org/10.1016/j.atmosenv.2008.08.002>, 2008.

839 Sisterson, D. L. and Frenzen, P.: Nocturnal boundary-layer wind maxima and the problem of wind power assessment., *Environ.*
840 *Sci. Technol.*, 12, 218–221, <https://doi.org/10.1021/es60138a014>, 1978.

841 Smalikho, I.: Techniques of wind vector estimation from data measured with a scanning coherent doppler lidar, *J. Atmospheric*
842 *Ocean. Technol.*, 20, 276–291, [https://doi.org/10.1175/1520-0426\(2003\)020<0276:TOWVEF>2.0.CO;2](https://doi.org/10.1175/1520-0426(2003)020<0276:TOWVEF>2.0.CO;2), 2003.

843 Stull, R. B.: An introduction to boundary layer meteorology, Springer Science & Business Media, 688 pp., 1988.

844 Su, L., Lu, C., Yuan, J., Wang, X., He, Q., and Xia, H.: Measurement report: the promotion of low-level jet and thermal-effect on
845 development of deep convective boundary layer at the southern edge of the taklimakan desert,
846 <https://doi.org/10.5194/egusphere-2024-1010>, 15 May 2024.

847 Su, T., Li, Z., and Kahn, R.: Relationships between the planetary boundary layer height and surface pollutants derived from lidar
848 observations over china: regional pattern and influencing factors, *Atmospheric Chem. Phys.*, 18, 15921–15935,
849 <https://doi.org/10.5194/acp-18-15921-2018>, 2018.

850 Su, T., Li, Z., and Kahn, R.: A new method to retrieve the diurnal variability of planetary boundary layer height from lidar under
851 different thermodynamic stability conditions, *Remote Sens. Environ.*, 237, 111519, <https://doi.org/10.1016/j.rse.2019.111519>,
852 2020.

853 Sun, J. and Ongsomwang, S.: Impact of multitemporal land use and land cover change on land surface temperature due to
854 urbanization in hefei city, china, *ISPRS Int. J. Geo-Inf.*, 10, 809, <https://doi.org/10.3390/ijgi10120809>, 2021.

855 Sun, Y., Yin, H., Liu, C., Mahieu, E., Notholt, J., Té, Y., Lu, X., Palm, M., Wang, W., Shan, C., Hu, Q., Qin, M., Tian, Y., and Zheng,
856 B.: The reduction in C2H6 from 2015 to 2020 over hefei, eastern China, points to air quality improvement in China,
857 *Atmospheric Chem. Phys.*, 21, 11759–11779, <https://doi.org/10.5194/acp-21-11759-2021>, 2021.

858 Tamarin-Brodsky, T. and Hadas, O.: The asymmetry of vertical velocity in current and future climate, *Geophys. Res. Lett.*, 46,
859 374–382, <https://doi.org/10.1029/2018GL080363>, 2019.

860 Tuononen, M., O'Connor, E. J., Sinclair, V. A., and Vakkari, V.: Low-level jets over utö, finland, based on doppler lidar observations,
861 *J. Appl. Meteorol. Climatol.*, 56, 2577–2594, <https://doi.org/10.1175/JAMC-D-16-0411.1>, 2017.

862 Vivone, G., D'Amico, G., Summa, D., Lolli, S., Amodeo, A., Bortoli, D., and Pappalardo, G.: Atmospheric boundary layer height
863 estimation from aerosol lidar: a new approach based on morphological image processing techniques, *Atmospheric Chem.*
864 *Phys.*, 21, 4249–4265, <https://doi.org/10.5194/acp-21-4249-2021>, 2021.

865 Wang, C., Zhou, J., Zhou, S., Zhang, Y., and Zhang, M.: Distribution characteristics of wind in anhui province during 1981 -2012,
866 *J. Arid Meteorol.*, 33, 236–243, [https://doi.org/10.11755/i.issn.1006-7639\(2015\)-02-0236](https://doi.org/10.11755/i.issn.1006-7639(2015)-02-0236), 2015a.

867 Wang, C., Jia, M., Xia, H., Wu, Y., Wei, T., Shang, X., Yang, C., Xue, X., and Dou, X.: Relationship analysis of PM_{2.5} and boundary
868 layer height using an aerosol and turbulence detection lidar, *Atmospheric Meas. Tech.*, 12, 3303–3315,
869 <https://doi.org/10.5194/amt-12-3303-2019>, 2019.

870 Wang, H., Li, Z., Lv, Y., Zhang, Y., Xu, H., Guo, J., and Goloub, P.: Determination and climatology of the diurnal cycle of the
871 atmospheric mixing layer height over Beijing 2013–2018: lidar measurements and implications for air pollution, *Atmospheric*
872 *Chem. Phys.*, 20, 8839–8854, <https://doi.org/10.5194/acp-20-8839-2020>, 2020.

873 Wang, L., Qiang, W., Xia, H., Wei, T., Yuan, J., and Jiang, P.: Robust solution for boundary layer height detections with coherent
874 doppler wind lidar, *Adv. Atmospheric Sci.*, 38, 1920–1928, <https://doi.org/10.1007/s00376-021-1068-0>, 2021.

875 Wang, M., Fang, X., Hu, S., Hu, H., Li, T., and Dou, X.: Variation characteristics of water vapor distribution during 2000–2008
876 over Hefei (31.9°N, 117.2°E) observed by L625 lidar, *Atmospheric Res.*, 164–165, 1–8,
877 <https://doi.org/10.1016/j.atmosres.2015.04.003>, 2015b.

878 Wang, M., Wei, T., Lolli, S., Wu, K., Wang, Y., Hu, H., Yuan, J., Tang, D., and Xia, H.: A long-term doppler wind LiDAR study of
879 heavy pollution episodes in western Yangtze River delta region, China, *Atmospheric Res.*, 310, 107616,
880 <https://doi.org/10.1016/j.atmosres.2024.107616>, 2024.

881 Wang, S., Wang, Q., Jordan, R. E., and Persson, P. O. G.: Interactions among longwave radiation of clouds, turbulence, and snow
882 surface temperature in the Arctic: a model sensitivity study, *J. Geophys. Res. Atmospheres*, 106, 15323–15333,
883 <https://doi.org/10.1029/2000JD900358>, 2001.

884 Wang, Y., Hu, H., Ren, X., Yang, X.-Q., and Mao, K.: Significant northward jump of the western Pacific subtropical high: The
885 interannual variability and mechanisms, *J. Geophys. Res. Atmospheres*, 128, e2022JD037742,
886 <https://doi.org/10.1029/2022JD037742>, 2023.

887 Wei, T., Xia, H., Hu, J., Wang, C., Shangguan, M., Wang, L., Jia, M., and Dou, X.: Simultaneous wind and rainfall detection by
888 power spectrum analysis using a VAD scanning coherent doppler lidar, *Opt. Express*, 27, 31235–31245,
889 <https://doi.org/10.1364/OE.27.031235>, 2019.

890 Wei, T., Xia, H., Wu, Y., Yuan, J., Wang, C., and Dou, X.: Inversion probability enhancement of all-fiber CDWL by noise modeling
891 and robust fitting, *Opt. Express*, 28, 29662, <https://doi.org/10.1364/oe.401054>, 2020.

892 Wei, T., Xia, H., Yue, B., Wu, Y., and Liu, Q.: Remote sensing of raindrop size distribution using the coherent doppler lidar, *Opt.*
893 *Express*, 29, 17246–17257, <https://doi.org/10.1364/OE.426326>, 2021.

894 Wei, T., Xia, H., Wu, K., Yang, Y., Liu, Q., and Ding, W.: Dark/bright band of a melting layer detected by coherent doppler lidar
895 and micro rain radar, *Opt. Express*, 30, 3654–3663, <https://doi.org/10.1364/OE.450714>, 2022.

896 Wei, T., Wang, M., Jiang, P., Wu, K., Zhang, Z., Yuan, J., Xia, H., and Lolli, S.: Retrieving aerosol backscatter coefficient using
897 coherent doppler wind lidar, *Opt. Express*, 33, 6832–6849, <https://doi.org/10.1364/OE.551730>, 2025.

898 Wei, W., Wu, B. G., Ye, X. X., Wang, H. X., and Zhang, H. S.: Characteristics and mechanisms of low-level jets in the Yangtze
899 River delta of China, *Bound.-Layer Meteorol.*, 149, 403–424, <https://doi.org/10.1007/s10546-013-9852-8>, 2013.

900 Wood, R., Wyant, M., Bretherton, C. S., Rémillard, J., Kollias, P., Fletcher, J., Stemmler, J., De Szoeko, S., Yuter, S., Miller, M.,
901 Mechem, D., Tselioudis, G., Chiu, J. C., Mann, J. A. L., O'Connor, E. J., Hogan, R. J., Dong, X., Miller, M., Ghate, V.,
902 Jefferson, A., Min, Q., Minnis, P., Palikonda, R., Albrecht, B., Luke, E., Hannay, C., and Lin, Y.: Clouds, aerosols, and
903 precipitation in the marine boundary layer: an ARM mobile facility deployment, *Bull. Am. Meteorol. Soc.*, 96, 419–440,
904 <https://doi.org/10.1175/BAMS-D-13-00180.1>, 2015.

905 Wyngaard, J. C.: Structure of the PBL, in: *Lectures on Air Pollution Modeling*, edited by: Venkatram, A. and Wyngaard, J. C.,
906 American Meteorological Society, Boston, MA, 9–61, https://doi.org/10.1007/978-1-935704-16-4_2, 1988.

907 Xia, H., Shentu, G., Shangguan, M., Xia, X., Jia, X., Wang, C., Zhang, J., Pelc, J. S., Fejer, M. M., Zhang, Q., Dou, X., and Pan,
908 J.: Long-range micro-pulse aerosol lidar at 1.5 μm with an upconversion single-photon detector, *Opt. Lett.*, 40, 1579–1582,
909 <https://doi.org/10.1364/OL.40.001579>, 2015.

910 Xia, H., Shangguan, M., Wang, C., Shentu, G., Qiu, J., Zhang, Q., Dou, X., and Pan, J.: Micro-pulse upconversion doppler lidar
911 for wind and visibility detection in the atmospheric boundary layer, *Opt. Lett.*, 41, 5218, <https://doi.org/10.1364/ol.41.005218>,
912 2016.

913 Xia H., Chen Y., Yuan J., Su L., Yuan Z., Huang S., and Zhao D.: Windshear detection in rain using a 30 km radius coherent doppler
914 wind lidar at mega airport in plateau, *Remote Sens.*, 16, 924, <https://doi.org/10.3390/rs16050924>, 2024.

915 Xue, L., Zhou, D., Huang, X., Lou, S., and Ding, A.: Climatological characteristics of cold fronts and their impacts on air quality
916 in cold seasons over the eastern China, *J. Geophys. Res. Atmospheres*, 127, e2022JD037488,
917 <https://doi.org/10.1029/2022JD037488>, 2022.

918 Yan, Y., Cai, X., Wang, X., Miao, Y., and Song, Y.: Low-level jet climatology of China derived from long-term radiosonde
919 observations, *J. Geophys. Res. Atmospheres*, 126, e2021JD035323, <https://doi.org/10.1029/2021JD035323>, 2021.

920 Yan, Y., Cai, X., Miao, Y., and Yu, M.: Synoptic condition and boundary layer structure regulate PM_{2.5} pollution in the Huaihe
921 river basin, China, *Atmospheric Res.*, 269, 106041, <https://doi.org/10.1016/j.atmosres.2022.106041>, 2022.

922 Yang, B., Finn, D., Rich, J., Gao, Z., and Liu, H.: Effects of low-level jets on near-surface turbulence and wind direction changes
923 in the nocturnal boundary layer, *J. Geophys. Res. Atmospheres*, 128, e2022JD037657, <https://doi.org/10.1029/2022JD037657>,
924 2023.

925 Yang, K., Cai, W., Huang, G., Hu, K., Ng, B., and Wang, G.: Increased variability of the western pacific subtropical high under
926 greenhouse warming, *Proc. Natl. Acad. Sci.*, 119, e2120335119, <https://doi.org/10.1073/pnas.2120335119>, 2022.

927 Yang, Y., Fan, S., Wang, L., Gao, Z., Zhang, Y., Zou, H., Miao, S., Li, Y., Huang, M., Yin, S. H. L., and Lolli, S.: Diurnal evolution
928 of the wintertime boundary layer in urban beijing, china: insights from doppler lidar and a 325-m meteorological tower,
929 *Remote Sens.*, 12, 3935, <https://doi.org/10.3390/rs12233935>, 2020.

930 Yin, J., Gao, C. Y., Hong, J., Gao, Z., Li, Y., Li, X., Fan, S., and Zhu, B.: Surface meteorological conditions and boundary layer
931 height variations during an air pollution episode in nanjing, china, *J. Geophys. Res. Atmospheres*, 124, 3350–3364,
932 <https://doi.org/10.1029/2018JD029848>, 2019.

933 Yuan, J., Xia, H., Wei, T., Wang, L., Yue, B., and Wu, Y.: Identifying cloud, precipitation, windshear, and turbulence by deep
934 analysis of the power spectrum of coherent doppler wind lidar, *Opt. Express*, 28, 37406, <https://doi.org/10.1364/OE.412809>,
935 2020.

936 Yue, M., Wang, M., Guo, J., Zhang, H., Dong, X., and Liu, Y.: Long-term trend comparison of planetary boundary layer height in
937 observations and CMIP6 models over china, *J. Clim.*, 34, 8237–8256, <https://doi.org/10.1175/JCLI-D-20-1000.1>, 2021.

938 Zhang, C., Ding, R., Xiao, C., Xu, Y., Cheng, H., Zhu, F., Lei, R., Di, D., Zhao, Q., and Cao, J.: Association between air pollution
939 and cardiovascular mortality in hefei, china: a time-series analysis, *Environ. Pollut.*, 229, 790–797,
940 <https://doi.org/10.1016/j.envpol.2017.06.022>, 2017.

941 Zhang, F., Zhang, Q., Du, Y., and Kong, H.: Characteristics of coastal low-level jets in the bohai sea, china, during the early warm
942 season, *J. Geophys. Res. Atmospheres*, 123, 13,763-13,774, <https://doi.org/10.1029/2018JD029242>, 2018.

943 Zhang, H., Zhang, X., Li, Q., Cai, X., Fan, S., Song, Y., Hu, F., Che, H., Quan, J., Kang, L., and Zhu, T.: Research progress on
944 estimation of the atmospheric boundary layer height, *J. Meteorol. Res.*, 34, 482–498, <https://doi.org/10.1007/s13351-020-9910-3>, 2020.

945 Zhang, L., Zhang, H., Li, Q., Wei, W., Cai, X., Song, Y., Mamtimin, A., Wang, M., Yang, F., Wang, Y., and Zhou, C.: Turbulent
946 mechanisms for the deep convective boundary layer in the taklimakan desert, *Geophys. Res. Lett.*, 49, e2022GL099447,
947 <https://doi.org/10.1029/2022GL099447>, 2022.

948 Zhang, Y., Zuo, Q., Wu, Q., Han, C., and Tao, J.: An integrated diagnostic framework for water resource spatial equilibrium
949 considering water-economy-ecology nexus, *J. Clean. Prod.*, 414, 137592, <https://doi.org/10.1016/j.jclepro.2023.137592>, 2023.

950 Zhao, P., Zhang, R., Liu, J., Zhou, X., and He, J.: Onset of southwesterly wind over eastern China and associated atmospheric
951 circulation and rainfall, *Clim. Dyn.*, 28, 797–811, <https://doi.org/10.1007/s00382-006-0212-y>, 2007.

952 Zhao, S., He, J., Dong, L., Qi, S., Yin, D., Chen, J., and Yu, Y.: Contrasting vertical circulation between severe and light air pollution
953 inside a deep basin: results from the collaborative experiment of 3D boundary-layer meteorology and pollution at the sichuan
954 basin (BLMP-SCB), *Bull. Am. Meteorol. Soc.*, 104, E411–E434, <https://doi.org/10.1175/BAMS-D-22-0150.1>, 2023.

955 Zhao, W. and Zou, Y.: Hefei: an emerging city in inland china, *Cities*, 77, 158–169, <https://doi.org/10.1016/j.cities.2018.01.008>,
956 2018.

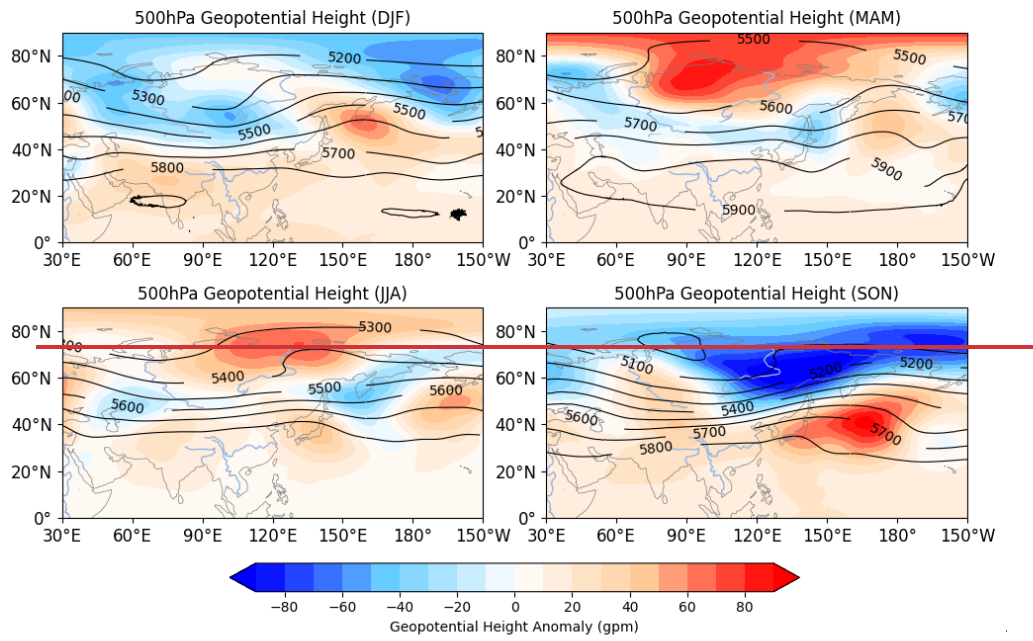
957 Zhou, J.: Lidar observations of asian dust over hefei, china, in spring 2000, *J. Geophys. Res.*, 107, 4252,
958 <https://doi.org/10.1029/2001JD000802>, 2002.

959
960 Zhu, F., Ding, R., Lei, R., Cheng, H., Liu, J., Shen, C., Zhang, C., Xu, Y., Xiao, C., Li, X., Zhang, J., and Cao, J.: The short-term
961 effects of air pollution on respiratory diseases and lung cancer mortality in hefei: a time-series analysis, *Respir. Med.*, 146,
962 57–65, <https://doi.org/10.1016/j.rmed.2018.11.019>, 2019.

963

964

Appendix A



965

966

967

Figure A1. Seasonal distributions of 500 hPa geopotential height (contour, units: gpm) and geopotential height anomalies (shaded, units: gpm).